ULg

UNIVERSITÉ de Liège

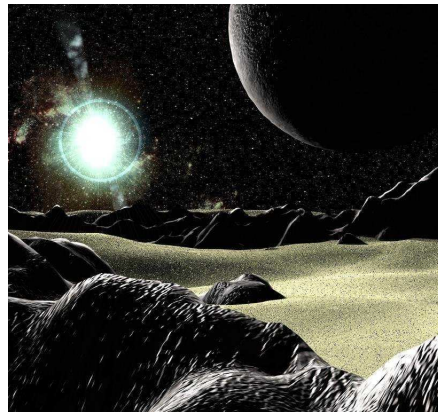# Université de Liège

Faculté des Sciences

Département d'Astrophysique, de Géophysique et d'Océanographie

Development of an iterative method
using the
MCS deconvolution algorithm

Application to gravitationally-lensed quasars

Artistic view of a quasar seen from a nearby planet.
Credit : Rolf Wahl Olsen.

Virginie Chantry

– June 2007 –

Contents

List of Figures

List of Tables

Chapter 1

Introduction

✮✮✮✮

It is no longer to be proved that gravitational lensing is a great source of information about galaxies, quasars, cosmology, ... Our interest goes to multiply-imaged quasars. The measurement of the time delay between several images of a gravitationally-lensed quasar allows a calculation of the Hubble constant H_0 [1] (Refsdal, 1966). This method is completely independent from classical methods based on "standard candles" [1] . Moreover, it has great advantages: it is basically geometrical and only General Relativity, which is now a well-established theory, is needed as theoretical support. The time delay between several images of a quasar has two components: a geometrical one and a potential one. These components depend on the mass distribution in the lens galaxy. This distribution can be constrained, to a large extent, by an accurate knowledge of the lensed images geometry: positions of these images in relation with the lens galaxy and possible presence of arcs or Einstein rings. Most of the time, the main uncertainty comes from the dark matter distribution in the lens galaxy.

The first stage is thus the modeling of the lensing system which eventually leads to the reconstruction of the source(s) undergoing the strong lensing. To do so, accurate astrometry and photometry are required not only for the multiple images, but also for the lensing galaxy. Therefore high resolution images are needed. The first instrument that comes to mind is obviously the NASA/ESA-HST or Hubble Space Telescope. In our particular case, the im-

---

[1] See definition in the glossary, page 83.

ages of gravitational mirages were acquired by the camera 2 of the instrument NICMOS (Near Infrared Camera and Multi-Object Spectrometer).

What matters next is of course the image processing. Even if we are dealing with high resolution images, it is very important. Indeed, the instrumental profile of the HST is far from having a simple shape: it contaminates any diffuse structure under or around the point sources. The technique used is the deconvolution with the MCS algorithm (Magain, Courbin & Sohy, 1998). It is based on the non violation of the sampling theorem: we try to obtain images with a better resolution instead of an infinite one. As a consequence of the knowledge of the final PSF or *Point Spread Function*, an image is decomposed into point sources and a diffuse background.

A new image processing using this algorithm has been developed. We call it the *iterative method*: the PSF is improved step by step by estimating the background and subtracting it from the original images. So it simultaneously allows us to determine the PSF and to perform a deconvolution of images containing several point sources plus extended structures. Therefore it is particularly well-suited for multiply-imaged quasars when no extra star is available in the field for the PSF determination.

The first object we investigate is the famous Cloverleaf, H1413+117, a quadruply-imaged quasar. Two sets of NIC-2 data are analyzed: the first one was obtained with the F160W filter and the second one with the F180M filter. The iterative method gives astrometric and photometric measurements in both filters and reveals the primary lensing galaxy as well as a partial Einstein ring. The reliability of the method is checked on a synthetic image similar to H1413+117.

The second gravitationally-lensed system under investigation is called WFI J2033-4723. In this case too we obtain accurate astrometric and photometric measurements in the F160W filter. We detect the lensing galaxy which, unlike the Cloverleaf, is already obvious on the original images, as well as an extended and faint background surrounding the lensed images.

The third lensed quasar is WFI J2026-4536. The F160W data provide accurate astrometry and photometry and allow an accurate analysis of the primary lens which is already observable on the original frames.

From the outset and to close this introduction, let me underline the fact that the deconvolution technique is far from being obvious and easy to apply. It requires more than common sense and scientific abilities: it deals with instinct and intuition. I would describe it as a mix between art and science, which makes it even more interesting in my eyes.

This piece of work is divided as follows: Chapter 2 presents the theoretical aspects needed to go through this report (quasars, gravitational lensing and deconvolution), the iterative process using the MCS algorithm is presented in

Chapter 3 and the application of this new method to several lensed systems is detailed in Chapter 4. We then conclude in Chapter 5 while Chapter 6 deals with the prospects of this work, i.e. modeling strong lenses.

Let us mention that this work was carried out in the context of a collaboration named *COSMOGRAIL*, which stands for COSmological MOnitoring of GRAvItational Lenses. Chapter 6 provides more details about it.

Chapter 2

Theoretical notions

Contents

2.1   Quasars

This section is mainly based on the following works: Krolik (1999), Binney
& Merrifield (1998) and Letawe (2006).

2.1.1   Introduction

Some galaxies show a strange behavior. What differs from classical ones is the
presence in their center of a nucleus releasing a huge quantity of energy by non
nuclear processes as it is the case in the stellar interior: these galaxies produce
very high luminosities (up to ten times the typical luminosity of a galaxy) in
tiny volumes. They are called *AGN* (see Fig. 2.1), which stands for *Active
Galactic Nuclei*, or simply active galaxies. They are observable in a wide
range of wavelengths and their spectra are very interesting: in the optical and
UV, they present emission (and sometimes absorption) lines reaching a flux
of several percent of the continuum flux. In most cases it is impossible (for
the moment...) to obtain an image with a resolved active nucleus. However
this is possible at radio frequencies. We can thus sometimes observe some
variable structures that seem to move at very high velocities. AGN are
also important to astrophysicists because they allow them to investigate the
cosmological evolution of galaxies and the intergalactic medium through the
absorption lines in the spectra of bright distant AGN (quasars, see Section
2.1.2).
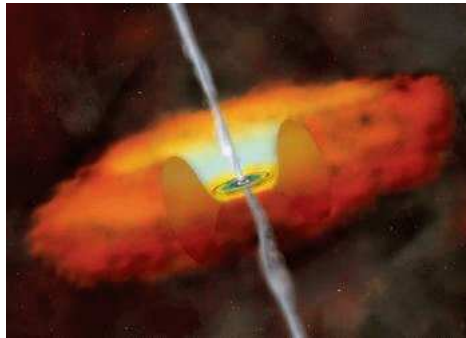
Figure 2.1: Artistic view of an AGN. The central black hole is surrounded
by a disk composed of hot gas and a huge belt composed of colder gas and
dust. The latter is called the *torus*. We can also see two jets of high energy
particles. Credit: CXC/M.Weiss.

AGN can be sorted out in four categories: Seyfert galaxies, radio galaxies,
blazars and quasars. The latter are the main subject of this chapter. Let us
explain briefly what the other types consist in.

Seyfert galaxies

Since galaxies are studied, some scientists have been observing some objects with unusual shapes. The best example is probably Carl Seyfert who made a catalog, back in 1943, with galaxies looking like spiral but having a very bright region at their center, i.e. a very bright nucleus, that often show quite broad emission lines of high excitation.

A very interesting characteristic of such galaxies, called without surprise *Seyfert* galaxies, is the tiny size of their nucleus. Indeed, this very bright part is highly variable on periods of less than a year. That deserves a short explanation. Let us assume that the luminosity of an extended object of size a doubles. These variations have to occur simultaneously on the entire nucleus: there must be an exchange of information between the different points of this nucleus. The observed brightness of the object adjusts to the new level in a time $\tau \simeq a/c$, i.e. in the time that light takes to travel from the back of the object to the front. It implies, as periods of several months are observed, that the maximal size of the nucleus cannot be larger than several light-months, which is really small compared to the size of the entire galaxy.

Seyfert galaxies are classified in two groups depending on the aspect of their spectrum. *Type I Seyfert* galaxies emit an intense continuum and in their spectra the permitted spectral lines have very broad wings while the forbidden lines are narrow because of a weaker Doppler effect. In *Type II Seyfert* galaxies both permitted and forbidden lines are less broadened by the Doppler effect. Moreover, they show a less intense continuum. One third of the Seyferts are of Type II.

The Seyfert phenomenon can also occur at lower luminosity. Indeed, some galaxies show a nucleus similar to the Type II Seyferts but the forbidden lines are caused by atoms in a lower ionization stage. They are called *LINERs* for *Low Ionization Nuclear Emission Line Regions*. Most of the time, LINERs reside in the center of elliptical galaxies.

Radio galaxies

Radio galaxies constitute another type of AGN. They differ from Seyfert galaxies because their nucleus is not necessarily visible. These objects, which most of the time look like normal elliptical galaxies, are characterized, as their name tells us, by strong and extended radio emissions, 10 000 times superior to those of classical galaxies.

These radio waves are produced by highly energetic electrons moving in a
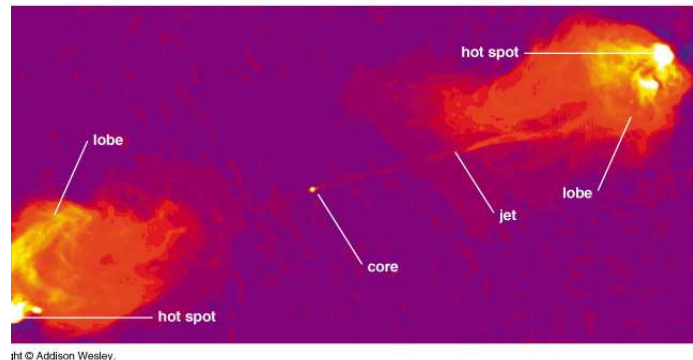
Figure 2.2: Radio lobes tied to the nucleus by thin relativistic jets. Credit: Addison Wesley.

magnetic field[1], i.e. by synchrotron radiation[2](see Fig. 2.3 for an illustration of this phenomenon). The radio flux comes from two huge regions called the *radio lobes* and located on either side of the nucleus. In general their size is about 10 times larger than the one of the galaxy and can reach several megaparsecs[2]. High-resolution radio images reveal that these lobes are often tied to the nuclear source by thin relativistic filaments called *radio jets* (see Fig. 2.2). Sometimes a jet can be visible at optical frequencies, as it was discovered by Geoffrey Burbidge in 1956 in the giant elliptical galaxy M87 (see Fig. 2.4). Radio galaxies whose emissions are dominated by the compact nucleus are called *FR-I* radio galaxies whose those which emissions are dominated by the lobes are called *FR-II* radio galaxies.

As for Seyferts, *FR-II* radio galaxies can be sorted out in two categories according to their optical spectrum:

- *narrow-line* radio galaxies or NLRGs, which show only the narrow emission lines that we find in Type II Seyferts;

- *broad-line* radio galaxies or BLRGs, which also show the broad lines observed in Type I Seyferts.

Blazars

The word *blazars* comes from *BL Lacertae*, the prototype of this class of objects, and obviously from the term *quasar* itself. Blazars are radio emitters

---

[1]This magnetic field is created by the particles moving in the accretion disk of the supermassive black hole.

[2]See definition in the glossary, page 83.
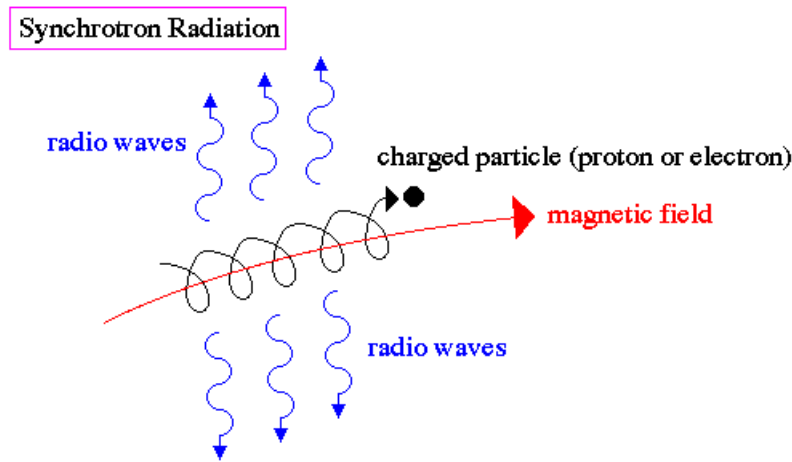
Figure 2.3: Illustration and explanation of the synchrotron radiation phenomenon. Credit: http://blueox.uoregon.edu.

and appear to be point-like, very bright and dramatically variable objects: they can change in brightness by large factors on timescales of a few weeks.

Blazars can be sorted out in two categories: *BL Lac* objects and *OVV* quasars, OVV standing for *Optically Violent Variables*. The difference resides in the fact that OVV show broad but weak optical emission lines in their spectra, which is characteristic of quasars, while BL Lac objects do not. Let us mention that the border between these two types is quite fuzzy. Depending on the moment of observation, a blazar can even switch from one category to the other.

At first it was believed that BL Lacertae was some kind of extremely variable star. But in 1974, Adams found out it is an AGN: the bright point source is actually surrounded by a faint nebulosity, i.e. an elliptical galaxy. The spectra revealed a redshift of 0.07 (Miller, French & Hawley, 1978) for this object.

Blazars are probably a particular case of radio galaxies, their characteristics being due to their relative position to the Earth: the latter is located on the axis of the jets and the radio lobes (see section 2.1.3 for further explanation). One of the arguments is the following: high resolution observations

Figure 2.4: The giant elliptical galaxy (E0 according to Hubble classification) M87, located at $50 \ 10^6$ light years, is an AGN. It corresponds to the radio source called *3C 274*. The galaxy itself appears to be red: it is composed of old and relatively cold stars. The blue radio jet, made of high energy electrons, comes from the nucleus and is around 6500 light years long. Credit: NASA/STScI.

show that blazars are located at the center of elliptical galaxies and radio galaxies are elliptical too.

2.1.2   Once upon a time...

The neologism *quasar* stands for *QUAsi-Stellar Astronomical Radio source* and was born in the late 1950s. This name was introduced when very loud radio sources were discovered. For some of them, no visible counterpart other than a stellar-looking object was observed. It was believed that quasars were some strange and new kind of stars belonging to the Milky Way. But their spectra showed very clear emission lines corresponding to no usual chemical element. This mystery was solved in 1963 by the Dutch astronomer Maarten Schmidt who studied a particular quasar, 3C 273, observed during the third radio sources survey carried out at Cambridge University[3]. According to him, quasars are very distant and, so, very bright sources. Therefore the emission lines are strongly redshifted (in this particular case the redshift z is equal to 0.16) and simply correspond to hydrogen. It means that 3C 273 is receding at a rate of around 47 000 km/s. More generally it shows that

---

[3]That is why each object disovered during this survey has a name which begins with "*3C*".

quasars are far from being located in our galaxy.

Later, it was found that many similar objects were radio-quiet, i.e. did not emit radio waves. These were called *Quasi-Stellar Objects* or *QSOs*. Nowadays, the term *quasar* is used for all of them even if only about 10 % of the QSOs known to date have been proved to radiate at least 0.1% of their total luminosity in the radio range.

Some spectral similarities to Type I Seyferts were also pointed out. It is now agreed that QSOs are no stars of the Milky Way at all, but objects located at the center of distant galaxies. Their nucleus is so bright optically that it can outshine the whole surrounding galaxy. At this center some sort of very energetic process is occurring, most likely due to the presence of a supermassive black hole.

So why are they point-like? Simply because of their distance. Indeed, they are so distant that their optical angular size is comparable to the resolution of ground-based observations. Indeed, at $z \simeq 1$ the angular size of an average galaxy amounts only to $1''$ [4]. The luminosity of the nucleus completely drowns the stellar light and from our planet the object appears as an unresolved point. It is only under very good observing conditions that the host galaxies of QSOs can be observed.

All host galaxies of QSOs which are strong radio emitters, i.e. *radio-loud* quasars, seem to be giant elliptical. It is less clear for QSOs which are not strong radio emitters, i.e. *radio-quiet* quasars: the distribution of luminosity of the host is better represented by the exponential law, the latter being typical of spiral galaxies. For AGN with a redshift larger than 1, it is quite rare to observe the host galaxy: the visible light we receive is ultraviolet in the rest frame and most galaxies are weak in these bands. Moreover, at such redshifts, the luminosity contrast between the host and the nucleus is very large.

Let us mention that the distinction between Seyferts and quasars is quite fuzzy. To make it clearer, it has been decided that AGN with absolute magnitudes brighter than $M_v \sim -23$ are considered as QSOs, and fainter radio-quiet objects as Seyferts. Another distinction is often made: if the host galaxy is visible we talk about a Seyfert galaxy. If none is visible, we talk about a quasar. Let us insist on the fact that this last distinction depends mostly on the background level and on the instrument performances but is somehow correlated to the luminosity of the object.

---

[4]Typically, $1''$ is the typical size of the seeing (see definition in the glossary, page 83) disk even at a good ground-based observatory.

2.1.3   The Unified Model of AGN
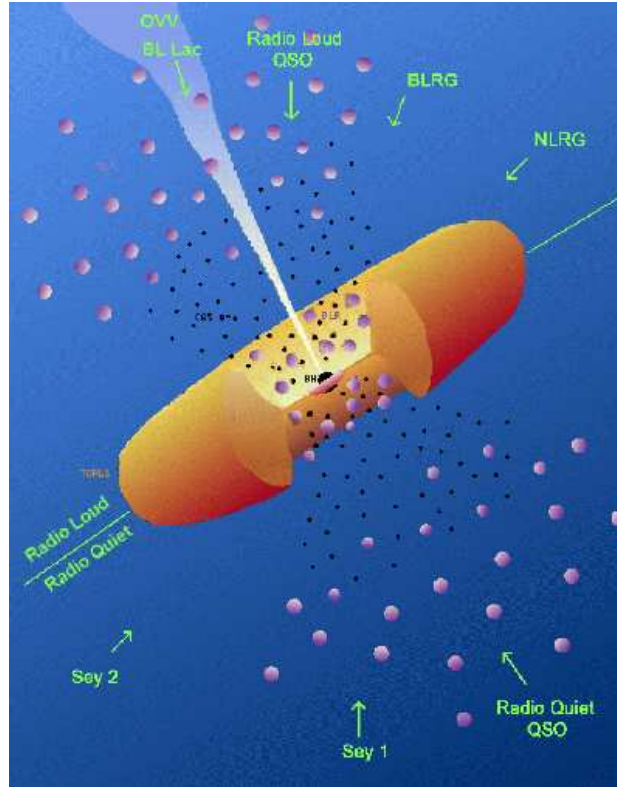
Figure 2.5: Schematic representation of how an active galactic nucleus looks like in the Unified Model paradigm, depending on the angle with the line of sight. Credit: M. Polletta, ITESRE/CNR, Bologna, Italy.

In the 1980s, unified models of AGN were developed. Nowadays a standard theoretical model is generally accepted to explain the existence of the whole AGN family. It is simply called the *Unified Model* (see Fig. 2.5). The basic principle is the following: every type of AGN is the same phenomenon, at various luminosities, observed with different viewing angles, which, combined with the anisotropy of the AGN radiation and a possible dust obscuration, can cause the apparent differences. Let us go a little bit further in this theory.

It is believed that the friction caused by matter falling into a supermassive black hole of between 10^6 $M_\odot$ and 10^9 $M_\odot$ is responsible for the huge energy release in AGN. As the angular momentum must be conserved, the matter flattens into an accretion disk (see Fig. 2.6). This matter is heated by friction and becomes a plasma which emits a strong continuum in the optical, UV
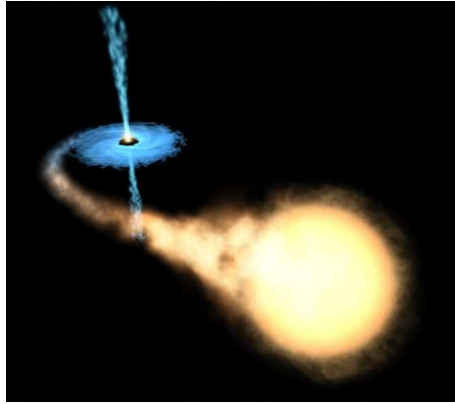
Figure 2.6: Artistic view of a black hole accreting a star. Credit: ESA, NASA and Felix Mirabel (French Atomic Energy Commission and Institute for Astronomy and Space Physics/Conicet of Argentina).

and X-ray bands. Let us notice that this continuous radiation is responsible for the excitation of the layers surrounding the black hole. This energetic process is much more efficient that nuclear reactions occurring in stars: an active galaxy can be as bright as several galaxies. That is why we can observe such objects even if they are located very far. The furthest AGN detected to date is situated at a redshift of 6.28.

The accretion disk is surrounded by a region containing clouds of dust orbiting around the black hole. These clouds are responsible for the spectral lines observed in active galaxies, which are, of course, affected by the Doppler effect. Moreover, the area around the black hole is divided in two different regions: the *broad-line region* (BLR), closer to the black hole, and the *narrow-line region* (NLR), further from the black hole. Indeed, clouds with a shorter orbital radius move faster than clouds with a larger one. As a consequence, their velocity dispersion is larger and so is the broadening of their emission lines.

The *torus* is a region surrounding the fast clouds but located in the same plane as the accretion disc. It consists in a thick belt of gas and dust, with a diameter of about 10^4 AU[5]. This region is opaque to visible or UV radiation.

Let us insist on the fact that the high density clouds are visible only if the line of sight is situated along a cone around the axis of symmetry of the torus. The lower the angle between the line of sight and the orbital plane, the less core emission reaches us because of the presence of the dust torus (see Fig. 2.7). When the broad-line region is observable, we are dealing with

---

[5]See definition in the glossary, page 83.
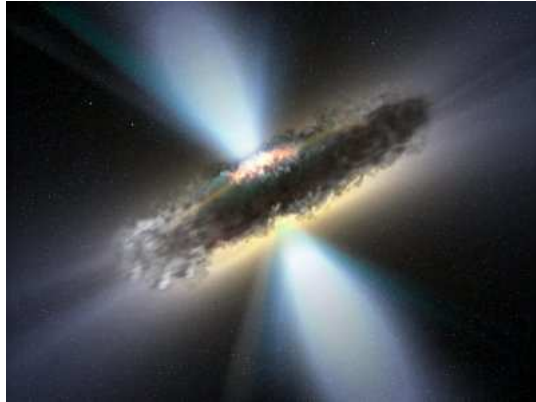
Figure 2.7: This artistic illustration shows the thick dust torus surrounding a supermassive black hole. As the line of sight is in the plane of the torus, most of the light emitted by the accretion disk is blocked. Credit: ESA/V.Beckmann (NASA-GSFC).

a QSO or a Type 1 Seyfert depending on the luminosity. When we cannot see this region, the spectrum is dominated by narrow emission lines and we are dealing with a Type II Seyfert. Still, in the latter case, some photons coming from the high density region can be scattered in our direction and broaden the wings of the narrow emission lines.

Perpendicular to the orbital plane and along the rotation axis, some particles are accelerated by a magnetic field (see Fig. 2.3 above) to velocities close to the speed of light. These relativistic particles form very long and thin jets which are responsible for the radio emission of some active galaxies. When these particles encounter some matter they are decelerated and we can observe *radio lobes*. In such a case the AGN is *radio-loud*. On the contrary, if no jets are observable, the AGN is *radio-quiet*. The reasons for the presence or absence of jets are still obscure.

In blazars the jets are pointing towards us and only a region with a small radius is observable. In radio galaxies, our line of sight does not pass right down the jets but they are seen on side. It is obvious now why blazars are much less likely than radio galaxies. Here also we can distinguish narrow-line and broad-line galaxies.

If the line of sight passes through the dust torus and if they are both included in the same plane, the BLR and the continuum are unobservable: we are in the presence of a Type II Seyfert or a Type II quasar (see next section), depending on the luminosity of the nucleus, or in the presence of a NLRG if the AGN is radio-loud. However, as already mentioned, a part of the continuum is still reachable to us: some photons responsible for it

are scattered and polarized by free electrons orbiting outside the dusty and obscure zone.

Let us go back to what is responsible for the existence of AGN, as first suggested by the British scientist, Donald Lynden-Bell, in 1969: supermassive black holes. To produce a luminosity typical to that of a quasar, i.e. 10^{40} W, a supermassive black hole would have to consume a quantity of matter equivalent to 10 stars like the Sun per year. For the brightest specimens this amount increases to 100 $M_\odot$. It is very likely that active nuclei "turn off" and "on", depending on their surroundings. That suggests that they will not keep on consuming the same amount of matter until the end of times: when a quasar has consumed all the matter in its sphere of influence it will become an invisible object and its host an ordinary galaxy. That explains the absence of nearby AGN and why they appear to have been much more common in the early Universe. That also means that most galaxies, including ours, could have gone through an active stage. They would be quiet now because the supermassive black hole would not be accreting in significant amounts any more. But if a galaxy with a quiet supermassive black hole enters in collision with another galaxy, some fresh material can enter the sphere of influence of the black hole and the quiet galaxy is back to the state of AGN. There may even be a connection between the brightness of an active galactic nucleus and the time since it was last gravitationally-disturbed.

To end this section let us insist on several important dark zones in the understanding of AGN. First of all, the model of the supermassive central black hole, even if it is the most commonly accepted, is not completely confirmed. Indeed, direct signatures of this monster are harder to obtain than some indirect ones. The most comprehensive and convincing argument was made by Rees & Ostriker in 1977 concerning the short variability timescales and the causality bounds, as already explained above. Then the origin of such black holes is quite unclear. Stars massive enough to collapse and give birth to such objects have never been observed. However it could be the result of a massive star that would have collapsed into a black hole, then the latter, accreting surrounding stars and matter, would have become larger and larger to finally form a supermassive black hole.

2.1.4   Properties of quasars

Nowadays, more than 60 000 quasars are known. The redshift extracted from their spectrum ranges from 0.06 to 6.4. That means that quasars are located at distances from 240 Mpc (780 million LY) to 4 Gpc (13 billion LY). It is not astonishing that they represent, to the eyes of the astrophysicists, a fascinating tool to probe the past of our Universe.

As quasars, though situated so far away from us, are observable, they have to be very bright. In fact they appear to be the most luminous objects known to date. Their luminosity can reach 10^{12} $L_\odot$. The quasar with the brightest apparent magnitude is 3C 273 in the constellation of Virgo. Its average apparent magnitude is 12.8 and its absolute magnitude is -26.7. Let us insist on the significance of such a value: located at a distance of 10 pc, 3C 273 would almost shine as our Sun. So this quasar is about 100 times more luminous than the average galaxies like the Milky Way.

A quasar spectrum presents an intense continuum from the X-ray to the IR range. In the optical and UV bands it shows narrow and broad emission lines. It was also pointed out that their spectrum is non thermal, i.e. it does not mainly depend on the temperature: their emission law does not follow Planck's Law for black bodies. As the Seyferts, quasars are divided in two subgroups depending on the presence of broad lines in their spectra: *Type 1* quasars show broad emission lines while *Type 2* do not. A typical spectrum of a Type 1 quasar is shown on Fig. 2.8.
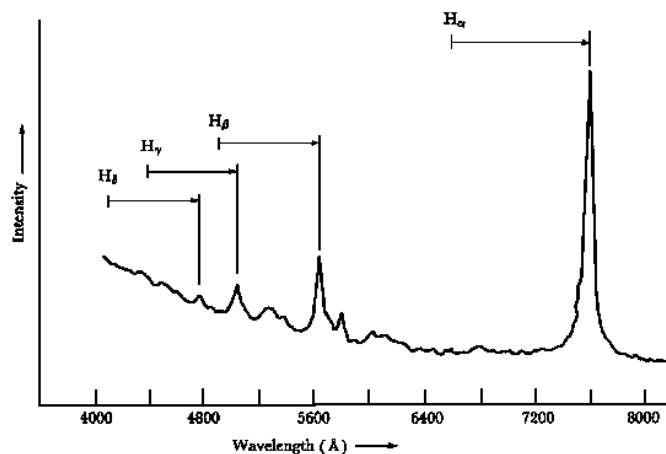
Figure 2.8: Typical spectrum of a Type 1 quasar. At short wavelengths, i.e. on the bluer side of the spectrum, the continuum is more intense. The redshifted emission lines of hydrogen (from the Balmer serie) are indicated. Credits: Jerrold G. Thacker, 2001.

2.2 Gravitational lensing

This theoretical section is mainly inspired by Schneider, Ehlers & Falco (1992), Binney & Merrifield (1998), Courbin (1999), Burud (2001) and Courbin & Minniti (2002).

2.2.1 Introduction

Another point making AGN so interesting for the scientific community is a phenomenon called *gravitational lensing* (see Fig. 2.9). Basically it is the bending of light rays coming from a distant bright source, such as a quasar, by a foreground object called *lens* and having a sufficiently deep gravitational well. The distorted and sometimes multiple images of such a distant source can be used to infer, amongst others, the mass-to-light distribution of the lens through its gravitational potential and to estimate its amount of dark matter. Lensing can also be used as a *gravitational telescope*: a lens concentrates the light from very faint and very distant (thus very old) background objects, making them appear brighter (it is called the *magnification effect*, see section 2.2.5 for further information) and therefore more easily investigated.
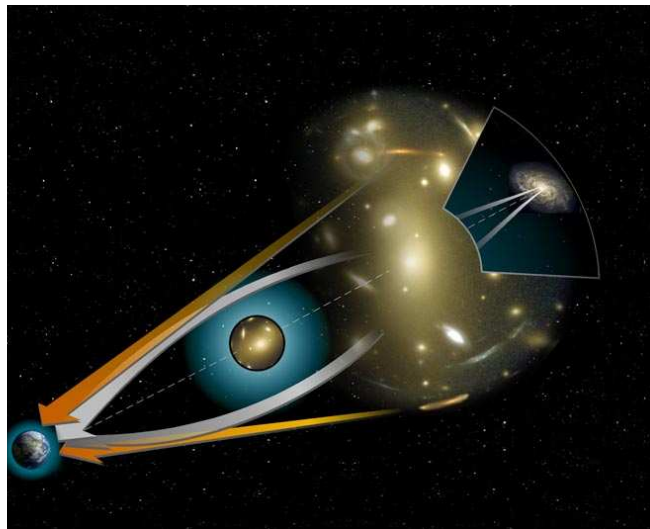
Figure 2.9: Illustration of the gravitational lensing phenomenon: the rays of light coming from a distant source are bent when passing around a massive object. The white arrows show the path of the light coming from the true source. In general several images of the source are observed in directions corresponding to the tangents of the real light rays, as shown by the orange arrows. Credit: NASA/ESA.

There are three classes of lensing:

1. *Strong lensing*: the distortions are particularly obvious. It occurs when a quasar is being lensed and multiply-imaged by a foreground galaxy. If the quasar is sufficiently variable, such a case can lead, through the measurement of the time delay (see section 2.2.6), to the determination of the Hubble constant which is crucial in cosmology.

2. *Weak lensing*: the distortions of background objects are much smaller. They can be found by studying statistically a large sample of objects. Indeed, the distortions can be seen as a stretching in a preferred direction, perpendicular to the line joining the distorted object to the center of the lens. It occurs, e.g., when galaxies are lensed by a foreground galaxy cluster. In such a case we can sometimes observe giant luminous arcs and arclets (which correspond to strong lensing). In studying the distribution of distortions we can measure the shear of the lensing field in any region and obtain an estimation of the mass distribution in the cluster.

3. *Microlensing*: no distortion in shape is observable but the light coming from the lensed object varies in time. It occurs when a star or quasar gets aligned with a massive and sufficiently compact foreground object. It leads to two distorted unresolved images resulting in an observable magnification. As the source, the lens and the observer move relative to each other, the configuration changes in time and so does the magnification. Galactic microlensing is very useful to detect compact halo objects in the Milky Way or extrasolar planets.

The effects are very small. Per example, in the case of strong lensing, a galaxy of 10^{11} $M_\odot$ will produce multiple images separated by at most a few arcseconds. Galaxy clusters can produce separations of several arcminutes.

Let us notice that gravitational lensing acts equally on all kinds of radiation: the phenomenon is not restricted to optical wavelengths; it is achromatic.

In the following sections we will concentrate on the topic under investigation in this work: multiply-imaged quasars which constitute a case of strong lensing.

2.2.2   A small piece of History

The first writings about the bending of light rays by a massive object go back to 1804 by Johann Soldner, a German mathematician and astronomer

working at the Berlin Observatory. In his article, entitled " On the deflection of a light ray from its straight motion due to the attraction of a world body which it passes closely ", he estimated, in a Newtonian context, the deflection angle of a light ray passing close to the solar limb to 0.84 arcsec. Let us note that, in the 18th century, Isaac Newton had already thought about that phenomenon but without finding a way to prove its existence or validity.

In 1911, Albert Einstein mentioned the influence of gravity on the propagation of light. He knew nothing about the work of Soldner one century earlier. But at the beginning of the 20th century, the Theory of General Relativity was incomplete and he obtained, for a star in the solar limb, the same deflection angle as Soldner estimated in the Newtonian context. He obtained the right value a little bit later, in 1912, when his General Theory of Relativity was finally complete. The deflection angle $\hat{\alpha}$ of a ray passing at a minimum distance ξ, also called the *impact parameter*, of an object of mass M is:

$$\hat{\alpha} \ = \frac{4GM}{c^2}\frac{1}{\xi} \tag{2.1}$$

where G is the constant of gravity and c the speed of light. This is equal to two times the Newtonian value. This factor of two reflects the spatial curvature. With the solar values for radius and mass, Einstein obtained $\tilde{\alpha}_{\odot} \ = \ 1.74''$.

In 1919, this theory was confirmed by Arthur Eddington who observed for the first time the apparent displacement of the position of a star in the solar limb during a total solar eclipse (see Fig. 2.10). In spite of the poor accuracy of his measurements, it proved that this deflection could only be explained in the context of a relativistic theory for the gravitation.
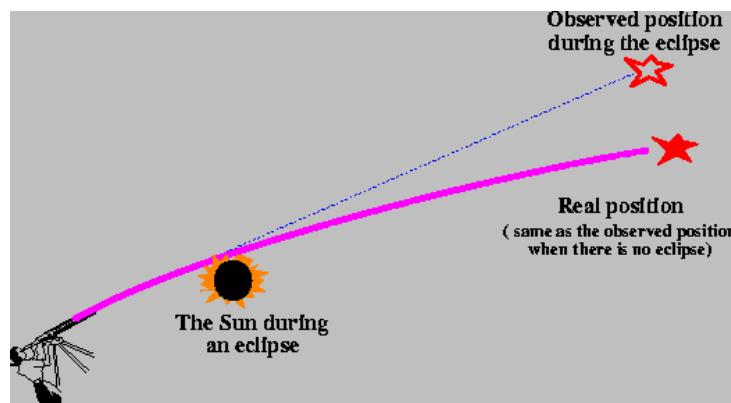
Figure 2.10: Bending of the light rays coming from a star in the solar limb during a total eclipse of the Sun. Credit: Jose Wudka.

Fritz Zwicky was the first to consider the case of galaxies acting as lenses in 1937. His calculations showed that this phenomenon was within the reach of observations as the probability that it could occur was of the order of 10%.

Originally, gravitational lensing was discussed for stars or galaxies but nothing else. Then, in the 1960's, the first quasars were discovered. A scientist called Barnothy was the first to connect them with lensing in 1965. From that moment, many other aspects of lensing were explored.

But it was not until 1979 that the first lensed quasar was discovered by Walsh et al.. They noticed that two apparently distinct quasars, separated by 6″, had nearly identical spectra and could be two images of the same object. Later, the lensing galaxy was identified and the lens nature of this system, named Q0957+561, firmly established. From that time, gravitational lensing had finally collected the attention it deserved and still does...

2.2.3   The lens equation

In the case of an extended gravitational lens, the deflection angle is not given by Eq. 2.1 anymore, which is only adapted to point mass lenses. Actually, every infinitesimal element of the mass distribution of the lens must be taken into account.

To give the expression of the deflection angle we must first describe the general context we work in. As, most of the time, the typical distances (to the source, to the lens, between the lens and the source) involved in the geometrical configuration of a lensed system are much larger than the size of a lensing galaxy, we work in the "thin lens approximation". That means that we always consider a mass sheet, perpendicular to the line of sight, containing all the deflecting matter. As a consequence, the latter is located at a single distance from the observer (and from the source). That is why we always consider a lens plane, an observer plane and a source plane as illustrated on Fig. 2.11. On the latter, O stands for *observer*, L for *lens*, S for *source* and I for *image*. D_L is the distance between the observer and the lens, D_S between the observer and the source and D_{LS} between the lens and the source. Several angles are also defined: $\hat{\alpha}$ is the deflection angle i.e. the angle (from the lens plane) between the direction of the source and the direction of the image, α is the angle between the source and its lensed image, β is the unlensed position angle and θ is the lensed position angle of the background source. Finally ξ is the distance, in the lens plane, of the light ray to the observer-lens axis.

The deflection angle $\hat{\alpha}$ for a lens with circular symmetry is given by:

$$\hat{\alpha}\left(\xi\right) \;=\; \frac{4GM\left(\xi\right)}{c^2}\frac{1}{\xi} \tag{2.2}$$

Observer plane   *Lens plane*   *Source plane*
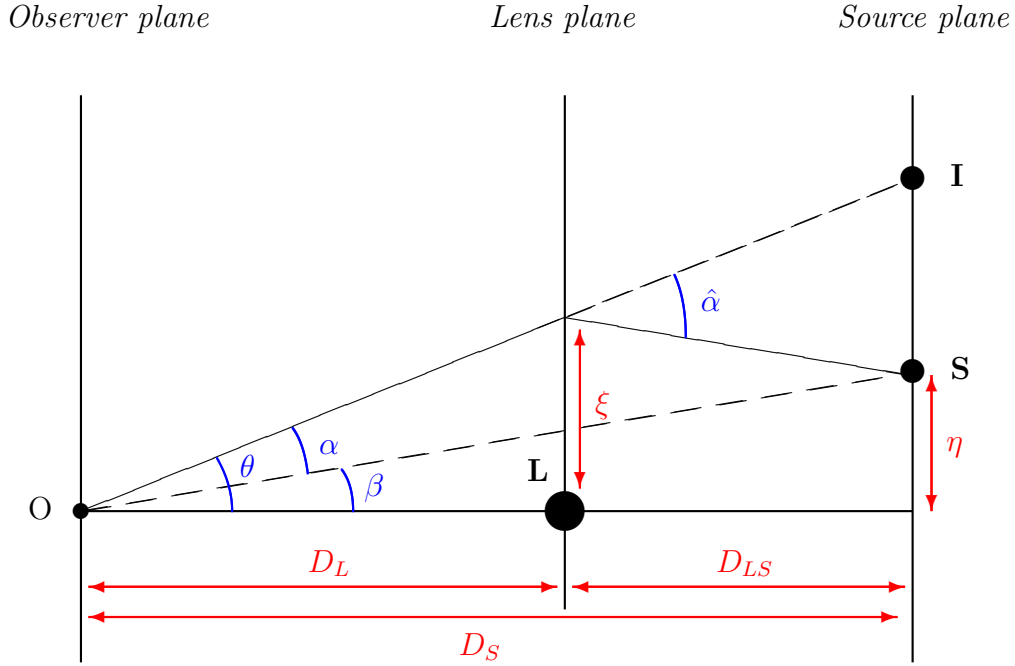
Figure 2.11: Geometry of a gravitationally-lensed system assuming the lensing galaxy L bends the light of a background source S. As a consequence the observer O sees a lensed image I of the source. The line passing through L and O is called the *optical axis* by similarity with an optical system.

where G is the constant of gravitation, $M(\xi)$ the mass contained in the radius ξ and c the speed of light. Let us consider that the angles involved in the lensed system are very small: θ, β, $\hat{\alpha} \ll 1$. In using formulae from basic trigonometry, it is easy to obtain the following equation:

$$\theta D_S = \beta D_S + \hat{\alpha} D_{LS}. \tag{2.3}$$

Let us define the reduced deflection angle $\alpha(\theta)$ as:

$$\alpha(\theta) = \frac{D_{LS}}{D_S} \hat{\alpha}(\theta). \tag{2.4}$$

The Eq. 2.3 then becomes:

$$\beta = \theta - \alpha(\theta). \tag{2.5}$$

As the observer has no direct access to the source, the observable is θ and not α.

If the mass distribution of the lens is not symmetric, Eq. 2.5 becomes vectorial:

$$\vec{\beta} \;=\; \vec{\theta} \,-\, \vec{\alpha}\left(\theta\right).$$ (2.6)

Let us insist on the fact that this equation is purely geometric: the energy or wavelength of the deflected light ray does not intervene in the reasoning. Gravitational lensing is indeed an achromatic phenomenon.

In the thin lens approximation, the deflection angle caused by any lens can be calculated in adding the contributions from every point mass contained in the lens plane. If we consider a two-dimensional vector $\vec{\xi} = (\xi_x, \xi_y)$ in the lens plane, we obtain the following expression:

$$\hat{\vec{\alpha}}(\vec{\xi}) \;=\; \frac{4G}{c^2} \int \int \frac{\Sigma(\vec{\xi'})(\vec{\xi}-\vec{\xi'})}{|\vec{\xi}-\vec{\xi'}|^2} \, d\vec{\xi'}$$ (2.7)

where $\Sigma(\vec{\xi})$ is the surface mass density at position $\vec{\xi}$. As $\vec{\theta} = \vec{\xi}/D_L$, we can write the reduced deflection angle for a finite circular lens with constant surface mass density Σ as:

$$\alpha\left(\theta\right) \;=\; \frac{4\pi G \Sigma}{c^2} \frac{D_L D_{LS}}{D_S} \, \theta.$$ (2.8)

In defining the critical surface mass density as follows:

$$\Sigma_{cr} \;=\; \frac{c^2}{4\pi G} \frac{D_S}{D_{LS} D_L} \;,$$ (2.9)

Eq. 2.7 finally becomes:

$$\alpha\left(\theta\right) \;=\; \frac{\Sigma}{\Sigma_{cr}} \, \theta.$$ (2.10)

It can be shown that a circular lens with uniform surface mass density acts as a perfect converging lens.

In general, for any mass distribution of the lens, multiple images are produced if $\Sigma \geq \Sigma_{cr}$.

In short, the challenge is to solve Eq. 2.8. Two situations can occur:

1. for a given mass distribution, you want to know the configuration of the images of the background source;

2. you try to find which mass distribution can be responsible for an observed configuration of lensed images.
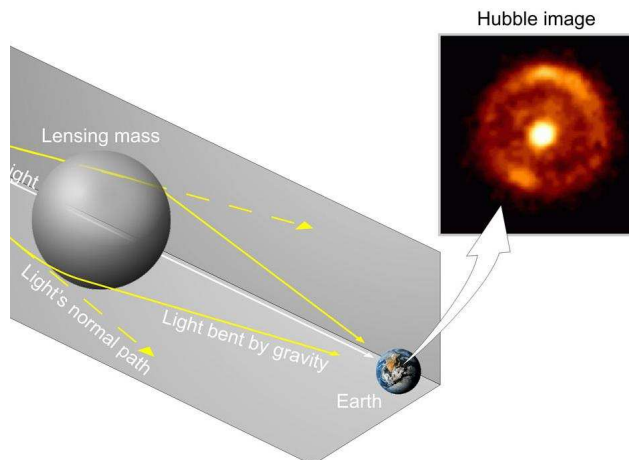
Figure 2.12: Illustration of the Einstein ring phenomenon and the necessary conditions to observe it. The image of the Einstein ring of B1938+666 was obtained with NICMOS, Near Infrared Camera and Multi-Object Spectrometer, on the Hubble Space Telescope, in 1998. Credit: L. J. King from University of Manchester.

2.2.4 Einstein rings

Unlike an optical lens, a gravitational one has no single focal point. As a consequence, if the observer, the massive lens and the background object are aligned, the latter will appear as a perfect ring surrounding the lens (see Fig. 2.12). This phenomenon was first mentioned by Chwolson in 1924 but then quantified by Einstein in 1936. That is why it is called an *Einstein ring*.

In such a case, the angle β (see Fig. 2.11) is equal to 0 and the lens equation (Eq. 2.6) is simplified and scalar:

$$\theta_E = \hat{\alpha}(\theta) \frac{D_{LS}}{D_S} \tag{2.11}$$

where θ_E is the angular radius of the Einstein ring. Introducing the expression of the deflection angle given in Eq. 2.2, the previous equation can also be written as follows:

$$\theta_E = \sqrt{\frac{4GM}{c^2} \frac{D_{LS}}{D_L D_S}}. \tag{2.12}$$

A lensed system showing an Einstein ring, complete or partial, leads to more accurate models of the mass distribution of the lens because it provides more constraints than a doubly or quadruply-imaged quasar. At very high

resolution it is even possible to resolve details of the ring, the latter being the amplified and distorted version of the quasar host galaxy.

In most cases the lensing galaxy is off-center, creating a number of images according to the potential of the lens and the relative positions of the observer, the lens and the source.

2.2.5 Magnification

When light is bent by a lens, the flux received is amplified compared to the one that we would observe if no lens was present: gravitational lensing conserves the surface brightness of a source but not the surface itself. That is why a lensed image of a source can be brighter than the source itself.

The magnification factor μ, i.e. the amplification of the image compared to the source, is thus equal to the ratio between the surface of the image and the surface of the source itself. For a circularly symmetric lens, it can be written as:

$$\mu = \frac{\theta d\theta}{\beta d\beta}.$$ (2.13)

For a point mass lens, Eq. 2.3 is a second degree equation and thus easy to solve. There are 2 solutions with opposite signs:

$$\theta_{\pm} = \frac{1}{2}\left(\beta \pm \sqrt{\beta^2 + 4\theta_E^2}\right).$$ (2.14)

So in the case of an isolated point mass lens, there are 2 lensed images. Let us notice that an image outside the ring defined by the Einstein radius θ_E has a *positive* parity, while an image inside has a *negative* one. In the latter case, the image has an inverted parity compared to the source, i.e. it is mirror inverted.

Differentiating Eq. 2.14 and taking Eq. 2.13 into account, we obtain the expression of the magnification for each image:

$$\mu_{\pm} = \frac{\sqrt{\beta^2 + 4\theta_E^2}}{\beta} + \frac{\beta}{\sqrt{\beta^2 + 4\theta_E^2}} \pm 2.$$ (2.15)

Let us introduce the impact parameter u. It is defined as the angular separation between the source and the lens in units of Einstein angle, i.e. $u = \beta/\theta_E$. Taking this new parameter into account, Eq. 2.15 becomes:

$$\mu_{\pm} = \frac{u^2 + 2}{2u\sqrt{u^2 + 4}} \pm \frac{1}{2}.$$ (2.16)

The flux magnification of the 2 images is obtained as follows:

$$\mu \;=\; |\mu_+| + |\mu_-| \;=\; \frac{u^2 + 2}{u\sqrt{u^2 + 4}}. \qquad (2.17)$$

2.2.6 An overview on time delays

A strong lens produces several images of the same background object. So the light that arrives on Earth has followed different paths: there is a delay between the arrival times of photons which have been emitted simultaneously but have travelled along the different paths. Assuming our quasar is sufficiently variable, a photometric monitoring with good time resolution will allow us to obtain the light curves of the lensed images. These light curves, as they come from images of the same source, should be identical apart from a shift in time. The latter is called a "time delay".

There are two contributions to the time delay. The first is the obvious delay due to the difference in optical length between two different paths. The second contribution is relativistic. It is due to the Shapiro effect. This effect occurs when light rays pass through regions with different gravitational potentials: the stronger the potential, the more the light will be slowed down. It is exactly what happens to light emitted by a quasar passing near a galaxy: different rays travel through different parts of the potential well. Let us mention that according to Fermat's principle[6], lensed images will occur at stationary points of the time delay.

In 1964, Sjur Refsdal wrote a paper presenting the first method to derive H_0 from time delay measurements. To do so a mass model for the lensing galaxy is needed. That topic will be briefly discussed in chapter 6. The possibility to probe our Universe and to get information about cosmology in studying time delays of lensed quasars has made them very famous and popular amongst the scientific community. Let us underline the fact that obtaining accurate values of H_0 from time delays is far from being easy. A first reason is that quasars rarely show very sharp variations. Photometric monitoring over long period, longer than the time delay, is then necessary. A second one is caused by microlensing of stars in the lensing galaxy. The microlensing variations will affect differently the individual light curves. If they occur on short time scales, they can be considered as an extra source of noise on the light curves. Conversely, if they occur on long time scales, they introduce trends into the light curves. The most critical case is probably

---

[6]Fermat's principle states that the optical path length must be extremal: it can be minimal or maximal but also a saddle point, the latter being a point of a function or surface which is stationary but not extremal.

when the microlensing variations occur on similar time scales as the quasar intrinsic variations. The third reason comes from the dominating source of error: it can vary from one case to the other. The main error can come from the time delay measurement, from the astrometry of the quasar images, from the modeling of the lens, from microlensing or even from some unknown systematic error. So, to obtain a reliable value of H_0, it is better to monitor as many systems as possible than to concentrate on a single one.

2.3   Deconvolution

The theoretical notions hereafter come mainly from the following PhD theses: Courbin (1999), Burud (2001) and Letawe (2006).

2.3.1   Introduction

Higher and higher resolution images are always demanded by scientists. Indeed, the more detailed are the observations, the more information they can provide. That is why it is very fashionable to build larger and larger telescopes and even to send some into space. But numerical techniques can also be used to improve data acquired with a not so big mirror, in not so good atmospheric and/or optical conditions. Deconvolution is one of these techniques allowing to recover information from blurred images. It has been largely developed after the launch of the Hubble Space Telescope because of strong optical aberrations discovered on its mirror.

Whenever some data are acquired, it is important to have within reach a good image processing technique to "clean" the observations. The first step is to get rid of parasites such as cosmic rays, cold or hot pixels, dead pixels, and so on. These effects are taken into account in every common reduction method. The second step consists in clearing the images from the influence of the optical system that has collected the light and possibly from the effects of the atmospheric turbulences. As already mentioned, deconvolution is one of the techniques used for this purpose.

Every observation $\mathcal{D}(\vec{x}, t)$ is sampled on a detector, $\vec{x}$ representing a pixel[7] on the Charged-Coupled Device[8] (hereafter CCD), and may depend on time t. It can be decomposed as follows:

$$\mathcal{D}(\vec{x}, t) = \left(\mathcal{F}(\vec{x}, t) \circledast \mathcal{T}(\vec{x}, t) \right) + \mathcal{N}(\vec{x}, t) \tag{2.18}$$

---

[7]The word *pixel* comes from the contraction of the words *picture* and *element*.

[8]See definition in the glossary, page 83.

where $\mathcal{F}(\vec{x}, t)$ represents the original signal, $\mathcal{T}(\vec{x}, t)$ stands for the instrumental profile and $\mathcal{N}(\vec{x}, t)$ is the noise. $\mathcal{T}(\vec{x}, t)$ is also called the total *PSF* or *Point Spread Function*. It is the instrumental diffraction shape of a theoretical point source of light through the whole optic system and possibly through atmospheric layers if the observations are ground-based. Let us notice that the noise $\mathcal{N}$ is mainly due to the readout of the CCD and to the statistical character of the counting of photons. The lower the signal-to-noise ratio (S/N) is, the poorer our estimate of the original signal will be.

To make it easier we will consider a unique observed image which does not depend on time. Equation 2.18 can then be written as follows:

$$\mathcal{D}(\vec{x}) = \Big(\mathcal{F}(\vec{x}) * \mathcal{T}(\vec{x}) \Big) + \mathcal{N}(\vec{x}). \tag{2.19}$$

Our aim is to recover the signal $\mathcal{F}(\vec{x})$ and to highlight high frequencies components on the data in spite of the noise. It is obvious that we have to deal with an inverse problem and, as a consequence of the presence of noise, with an ill-posed problem: it has no unique solution. Regularization, a process consisting in introducing additional information about the problem, is then necessary in order to select a solution amongst the set of all light distributions compatible with the observation, within the error bars.

Many different deconvolution techniques have been elaborated, each one being based on a different regularization criterion. Most of them present some weaknesses. At some level they all produce deconvolution artifacts, which add to the deconvolved image information that does not exist in the original one. This often prevents from obtaining reliable astrometric and photometric measurements. The next section will expose briefly three of the most used techniques and their problems.

2.3.2 The common methods and their weaknesses

Extremely brief reminder on convolution

Convolution is a mathematical operator, symbolized by $*$, which, when applied to two functions f and g [9], produces a third function which somehow represents the amount of overlap between f and a reversed and translated version of g. Mathematically, this phenomenon can be expressed by the following integral:

$$(f * g)(x) = \int_{-\infty}^{+\infty} f(\xi) \, g(x - \xi) \, d\xi. \tag{2.20}$$

---

[9]For simplicity we assume that they are both defined from $-\infty$ to $+\infty$.

Wiener deconvolution

The foundations of deconvolution techniques and time-series analysis were largely built by Norbert Wiener in a book that he wrote during but published after World War II. Wiener deconvolution is a linear procedure based on the application of the *Wiener filter* to reduce the noise problems inherent to deconvolution.

By the convolution theorem, which states that a convolution in the image space becomes a simple product in the Fourier space, we can apply the Fourier transform to Eq. 2.19 such that we obtain:

$$D(\vec{\nu}) = F(\vec{\nu}) \cdot T(\vec{\nu}) + N(\vec{\nu}) \tag{2.21}$$

where $\vec{\nu}$ is the variable in the Fourier space and where $D(\vec{\nu})$, $F(\vec{\nu})$, $T(\vec{\nu})$ and $N(\vec{\nu})$ are the Fourier transforms of $\mathcal{D}(\vec{x})$, $\mathcal{F}(\vec{x})$, $\mathcal{T}(\vec{x})$ and $\mathcal{N}(\vec{x})$ respectively.

What comes then to mind is to invert Eq. 2.21 to directly obtain the original signal in the Fourier space:

$$F(\vec{\nu}) = \frac{D(\vec{\nu}) - N(\vec{\nu})}{T(\vec{\nu})} \tag{2.22}$$

which is valid if $T(\vec{\nu})$ differs from zero. However the term $N(\vec{\nu})/T(\vec{\nu})$ diverges at high frequencies, precisely the ones we try to recover.

A solution to this problem was found by Wiener: before inverting the observed signal, one can apply a special filter to the data which will attenuate high frequencies. That filter can be written as follows in the Fourier Space:

$$\Phi(\vec{\nu}) = \frac{|B(\vec{\nu})|^2}{|B(\vec{\nu})|^2 + |N(\vec{\nu})|^2} \tag{2.23}$$

where $B(\vec{\nu}) = F(\vec{\nu})\, T(\vec{\nu})$. If there is no noise, the filter becomes equal to unity and has no effect on the observed signal. Of course, nor $N(\vec{\nu})$ neither $B(\vec{\nu})$ are known, but $|N(\vec{\nu})|^2$ and $|B(\vec{\nu})|^2$ can be estimated by separating the contributions from the noise and the actual data in the power spectrum of the data $|D(\vec{\nu})|^2$.

The maximum entropy methods

Here again we are willing to obtain a deconvolved signal that will be the best representation of the original signal in a least squares sense [10] . We are thus trying to minimize the following expression:

$$\left| \mathcal{D}(\vec{x}) - [\mathcal{F}(\vec{x}) * \mathcal{T}(\vec{x})] \right|^2. \tag{2.24}$$

---

[10]See definition of the *least squares minimization* in the glossary, page 83.

Let us assume that our CCD has only one dimension. We can write the previous expression in terms of a χ^2:

$$\chi^2 = \sum_{i=1}^{N} \left[\frac{d_i - \left(\Sigma_{j=1}^{N} t_{ij} f_j \right)}{\sigma_i} \right]^2 \qquad (2.25)$$

where N is the total number of pixels, σ_i an estimated value of the standard deviation of the signal acquired in the ith pixel, d_i the measured value in the ith pixel of the observed image and t_{ij} the intensity in pixel j of the PSF centered on pixel i.

Just before the 1950s, Shannon showed that the average amount of information contained in a probability distribution p_i is measured by the entropy:

$$\mathcal{H} = - \sum_{i=1} p_i ln\ p_i \qquad (2.26)$$

Moreover, the maximum entropy principle states that, amongst all the solutions to an inverse problem, the one with the highest entropy and, thus, the minimum amount of information, should be chosen. To apply it to image processing, we assume that the intensity distributions are normalized, e.g.:

$$\sum_{i=1}^{N} f_i = 1 \qquad (2.27)$$

so that f_i can be viewed as a probability, i.e. the probability that the next photon will be emitted in the region of the sky corresponding to pixel i.

The maximum entropy method consists in minimizing the following function which depends on N variables (the f_i):

$$\Phi = \chi^2 - \lambda \mathcal{H} \qquad (2.28)$$

where χ^2 is given by Eq. 2.25 and where λ is a Lagrange parameter introduced to modulate the weight of $\mathcal{H}$, which can be seen as a smoothing term. The maximum entropy image is the flattest (in other words, the closest to a constant) which is compatible with the data. Finally let us note that this method automatically constrains every f_i to be positive as expected for a detected number of photons.

The Richardson-Lucy algorithm

The Richardson-Lucy algorithm, created by Richardson in 1972 and theoretically developed by Lucy in 1974, is an iterative and non-linear procedure

which basic idea is to calculate the most likely f_j, given the observed d_i and known t_{ij}. If the noise is neglected in a first approximation, some manipulations of Eq. 2.19 lead to the following expression:

$$f_j^{(n+1)} = f_j^{(n)} \sum_{i=1}^{N} \frac{d_i}{c_i} t_{ij} \tag{2.29}$$

where f_j^n is the nth estimate of f_j, where

$$c_i = \sum_{k=1}^{N} t_{ik} f_k^{(n)}, \tag{2.30}$$

and where d_i/c_i is the ratio of the value acquired in pixel i and the value obtained in the same pixel from the image reconstructed after deconvolution. This ratio is then convolved by the normalized PSF t_{ij} to get rid of the details with higher frequencies than the instrumental profile. The so modified ratio is then used to correct the first estimation of the deconvolved image: we obtain a new estimation of f_j which can be used as a starting point for the next iteration. If this process converges, it converges to the maximum likelihood solution for f_j. Usually $f_j^{(0)}$ is the measured value in pixel j.

Let us notice that for positive data, a positive PSF, and a positive first approximation of the deconvolved image, every following estimation of fj will also be positive.

Their weaknesses

Mainly there are three problems encountered by these classical methods. The first one is related to the sampling theorem, the second one to the smoothing parameter and the last one to the positivity constraint. Hereafter we develop the three of them.

- *The sampling theorem*

  The sampling theorem states that a signal, continuous in time, can be reconstructed from its samples only if it is band-limited, e.g. its Fourier transform is equal to zero above a certain finite frequency ν_f, and if the sampling rate exceeds the so-called Nyquist frequency, written ν_c for *cut-off* frequency, equal to twice ν_f. When the sampling frequency is too low, all the components of frequencies higher than ν_c are badly represented by the chosen sampling step and superimposed on frequencies between $-\nu_c$ and ν_c. This artifact is called *aliasing*[11] (see fig. 2.13).

---

[11]Signals having the same sample as the original signal are called *aliases*.
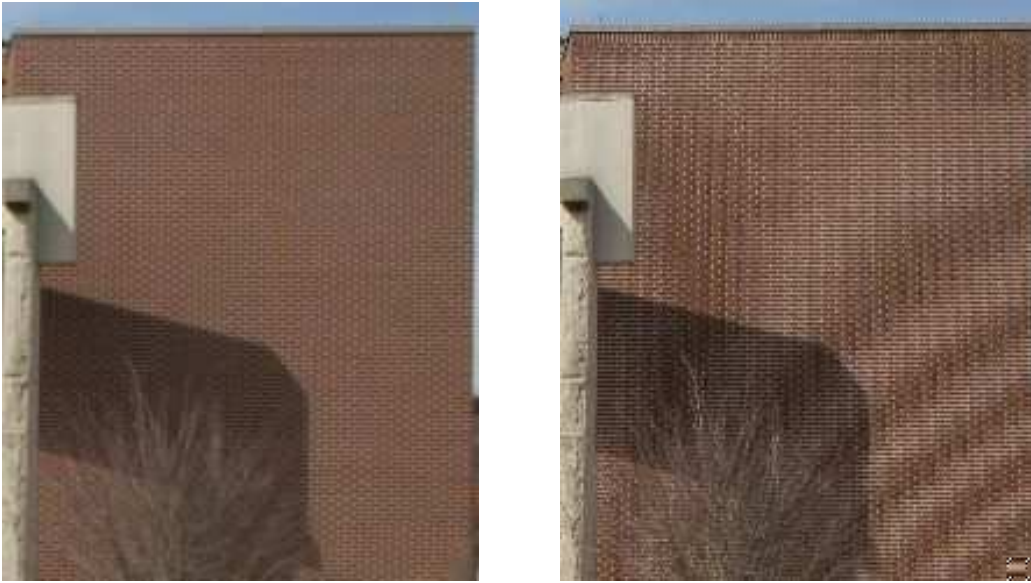
Figure 2.13: An example of the aliasing phenomenon. *Left*: properly sampled image of a brick wall. *Right*: effect of a bad sampling (undersampling) on the same image. The aliasing phenomenon is obvious. Credit: www.wikipedia.org.

Let us insist on the fact that, even if the d_i are well sampled, it does not imply that the f_i will be well sampled too. The simplest example of a violation of the sampling theorem is a perfect deconvolution of an image containing a star: it would give an image of the star narrower than the sampling step and this is not permitted. The problem of classic algorithms is that they attempt to reach an infinite resolution. That would be possible only if the pixel size of the detector was infinitely small, which is far from being the case. This is thus in complete contradiction with the sampling theorem. As a consequence, the *Gibbs phenomenon*, i.e. rings surrounding point-like objects, will appear in the deconvolved frame. This phenomenon, also known as *ringing artifacts*, comes from the fact that the signal is band-limited. We will not give more details about this special topic. Let us just insist on the fact that these artifacts are caused by high frequencies contained in the point sources. For those who are interested, here is a good reference of a PhD thesis developing this subject: Blanchet (2006).

- *The smoothing parameter*

  Usual algorithms select the smoothest solution amongst the ones com-

patible with the observed light distribution, according to different criteria: it allows them to attenuate the amplification of the noise and the Gibbs' oscillations. But choosing the smoothest image is in complete contradiction with our expectations. Indeed, our intuition tells us that an astronomical observation is far from being smooth: we want to detect objects like stars, planets, quasars, and other structures. We expect bright points on a faint diffuse background.

- *The positivity constraint*

  To be efficient, the positivity constraint must be applied to an image with no sky background. But most of the time, the photon noise implies a lot of pixels with a negative value. The algorithms such as Richardson-Lucy have to put to zero these negative values before deconvolution, in the observed frame as well as in the PSF. That modifies consequently the shape and the intensity of faint objects, as well as the wings of the instrumental profile.

A first step towards the solution was made by Lucy in 1993. He developed a technique based on the Richardson-Lucy algorithm and called the *PLUCY algorithm*. Its particularity resides in the decomposition of the deconvolved frame in 2 images, one containing the point sources and the other the diffuse background. High frequencies are thus treated separately. This allows less contamination of the deconvolved image by the ringing artifacts. This algorithm works better than the Richardson-Lucy method. However a fundamental weakness persists: the algorithm tries to obtain a deconvolved image with an infinite resolution, which is completely forbidden by the sampling theorem.

2.3.3   The MCS algorithm and its advantages

The basic principle of the MCS algorithm (Magain et al., 1998) is to respect the sampling theorem in trying to improve the spatial resolution of images instead of trying to obtain an infinite one. To do so we do not deconvolve the image by the total PSF $\mathcal{T}(\vec{x})$ but by a narrower one, $\mathcal{S}(\vec{x})$, so that the deconvolved frame has its own PSF $\mathcal{R}(\vec{x})$ compatible with its own sampling step:

$$\mathcal{T}(\vec{x}) = \mathcal{R}(\vec{x}) \ast \mathcal{S}(\vec{x}). \qquad (2.31)$$

Practically, $\mathcal{R}(\vec{x})$ is chosen so that the deconvolved data are well sampled: the image of a point source on the detector must have at least two pixels as full-width-at-half-maximum (hereafter FWHM). The same conditions prevail for the image of a point source in the deconvolved frame.

There are two important consequences of Eq. 2.31. First of all, the deconvolved image will be well sampled and its spatial resolution can be strongly improved. Secondly, the final instrumental profile of a point source, $\mathcal{R}(\vec{x})$, is known and even chosen by the user (generally it is a Gaussian function). We can also notice that the highest frequencies are modeled analytically. It allows us to decompose every astronomical image in a sum of M point sources and a diffuse background.

The shape of the point sources in the deconvolved frame is known but we will have to measure their intensity a_k and their center $\vec{c}_k$. So, if the detector is a square with N pixels on each axis, there are $3M + N^2$ variables, one intensity and two coordinates per point source plus one value of the background per pixel. The deconvolved image can thus be written as:

$$\mathcal{F}(\vec{x}) = \mathcal{H}(\vec{x}) + \sum_{k=1}^{M} a_k \mathcal{R}(\vec{x} - \vec{c}_k) \tag{2.32}$$

where $\mathcal{H}(\vec{x})$ is the background.

Practically, the algorithm attempts to minimize the following function:

$$\begin{aligned}
\mathcal{K} &= \sum_{i=1}^{N} \frac{1}{\sigma_i^2} \Big[\sum_{j=1}^{N} s_{ij} \Big(h_j + \sum_{k=1}^{M} a_k r(\vec{x}_j - \vec{c}_k) \Big) - d_i \Big]^2 \\
&+ \lambda \sum_{i=1}^{N} \Big[h_i - \sum_{j=1}^{N} r_{ij} h_j \Big]^2,
\end{aligned} \tag{2.33}$$

d_i being the value registered in pixel i on the CCD. The parameter λ allows the user to adjust the value of the χ^2 so that the deconvolved frame is statistically compatible with the observed data. Indeed, a least squares minimization is considered as good if $\chi^2 = 1$ per degree of freedom. Here again, if the detector is a square with N pixels on each axis, χ^2 must be approximately equal to N^2 so that the fit is considered as good. In other words, λ gives a weight to the smoothing term. The latter contains all the frequencies of the diffuse background higher than the one of $\mathcal{R}(\vec{x})$. Every structure with such a frequency is not physical so it has to be minimized. Finally the length scale of the smoothing is not arbitrary, as it is the case for most of the methods, but directly related to $\mathcal{R}(\vec{x})$ and, as a consequence, local.

The user is guided by the value of the χ^2 but also by the *residual maps*. The residual map $\mathcal{Z}(\vec{x})$ of an observation is expressed in units of standard deviation. It is defined as follows:

$$\mathcal{Z}(\vec{x}) = \frac{\mathcal{M}(\vec{x}) - \mathcal{D}(\vec{x})}{\sigma(\vec{x})} \tag{2.34}$$

where $\mathcal{M}(\vec{x})$ stands for the solution reconvolved by the partial PSF $\mathcal{S}(\vec{x})$[12]. It represents the deviation of the model compared to the original image.

It is also practical to work with the *reduced chi square* χ_r^2 measured on what we call the *reduced residual map*. Actually the latter expression is a misuse of language introduced to ease the communication. The reduced chi square of an image with N pixels is mathematically defined as follows:

$$\chi_r^2 = \frac{1}{N} \left(\frac{\mathcal{M}(\vec{x}) - \mathcal{D}(\vec{x})}{\sigma(\vec{x})} \right)^2. \tag{2.35}$$

Theoretically the χ_r^2 must be close to unity. That would be the case for a perfect deconvolution executed with a perfect PSF. If it is lower than 1, the model follows too closely the data and the deconvolution is noisy. This is called *overfitting*.

Another advantage of the MCS algorithm: it does not need the positivity constraint to be efficient. One can choose whether to use it or not depending on the case treated.

To end this section, let us mention that, as the MCS method is an iterative procedure, the user has to estimate the initial intensity and position of every point source in the image. The algorithm will adjust them during the process. Moreover, the MCS method preserves the astrometric and photometric properties of the observed objects. For readers who want more details about it, we suggest the original paper of Magain et al. (1998).

The analytical model

The MCS algorithm has other possibilities that we have not mentioned here. Amongst them, one is of great interest for us: the possibility of introducing an analytical model (considered as a part of the diffuse background) to fit the luminosity profile of a galaxy. We have two possibilities: a *de Vaucouleurs* model (de Vaucouleurs, 1948) well-suited for elliptical galaxies, i.e. bulge systems, and an *exponential* luminosity profile (Freeman, 1970) well-adapted to spiral galaxies, i.e. disk systems.

The light profile G of a galaxy with elliptical isophotes can be expressed as follows in the frame of the observed galaxy if the ellipse is centered on $(0, 0)$:

$$G'(x', y') = I_0 \; e^{-(Ax'^2 + By'^2 + Cx'y')^\alpha} \tag{2.36}$$

where I_0 is the central intensity of the galaxy, A, B and C are parameters of the model and where α is equal to 0.125 in the case of a de Vaucouleurs

---

[12]The solution must be reconvolved by $\mathcal{S}(\vec{x})$ and not by the total PSF $\mathcal{T}(\vec{x})$ because the deconvolved frame has its own PSF $\mathcal{R}(\vec{x})$.

profile and to 0.5 in the case of an exponential profile. If we choose the ellipse axes as the coordinate axes:

$$G(x,y) = I_0 \; e^{-\left(\frac{x^2}{a} + \frac{y^2}{b}\right)^{\alpha}} \tag{2.37}$$

where a is the semi-major axis and b the semi-minor axis of the ellipse.

There are other important parameters: the angle θ representing the orientation of the observed frame compared to the orientation of the ellipse, and the ellipticity e corresponding to the ratio between the minor and major axes. The angle θ leads to the *position angle* or PA which is the angle that folds back the semi-major axis of the ellipse on the direction of the North.

These parameters are related to the coefficients A, B and C:

$$a^2 = \frac{2cos(2\theta)}{(A+B)\;cos(2\theta) + A - B}, \tag{2.38}$$

$$b^2 = \frac{2cos(2\theta)}{(A+B)\;cos(2\theta) + B - A}, \tag{2.39}$$

$$\theta = \frac{1}{2}\;arctg\left(\frac{C}{B-A}\right), \tag{2.40}$$

$$e = \frac{B-A}{(A+B)\;cos(2\theta)}. \tag{2.41}$$

Another parameter that we can derive from the ellipticity is the inclination angle i of the galaxy on the line of sight (assuming it would have circular isophotes if seen face-on):

$$e = cos(i). \tag{2.42}$$

Let us add that the de Vaucouleurs' law can also be written as follows:

$$I(r) = I_e \; e^{-7.67\left(\sqrt[4]{\frac{r}{R_e}} - 1\right)} \tag{2.43}$$

where R_e is the projected effective radius, i.e. the radius which encloses half of the luminosity emitted by the galaxy, and I_e is the surface brightness at R_e.

Optimal image combination

The MCS algorithm has another considerable advantage: it allows the user to simultaneously deconvolve several images of the same field of view. Each image has its own partial PSF. The extended structures and the positions of the point sources are forced to be equal in each frame. For the intensity of the sources, the user can choose whether to force them to be proportional in each frame or not. If the data have been acquired consecutively during a

short time period then there is no physical reason to let the intensities vary from one deconvolved frame to the other. On the contrary, if the images were acquired over a long time period and with the purpose of determining the variations of intensity, then it is essential to let them vary from one frame to the other. The best example is probably the deconvolution of images of gravitationally-lensed systems in order to determine a time delay.

After a simultaneous deconvolution, the user obtains a unique and optimally constrained deconvolved image, which is compatible with and based on all the images of a same object taken in different observational conditions but in a given instrument configuration, e.g. through a given filter. That means that their total signal is used to constrain the parameters.

In the case of a simultaneous deconvolution of n images $\mathcal{D}_1(\vec{x})$, $\mathcal{D}_2(\vec{x})$, ..., $\mathcal{D}_n(\vec{x})$, each one of them having its own PSF $\mathcal{S}_1(\vec{x})$, $\mathcal{S}_2(\vec{x})$, ..., $\mathcal{S}_n(\vec{x})$, the function to be minimized is the following:

$$
\begin{aligned}
\mathcal{K} \;=\; & \sum_{i=1}^{N} \frac{1}{\sigma_{1,i}^2} \left[\sum_{j=1}^{N} s_{1,ij} \Big(\alpha_1 h(\vec{x}_j + \vec{\delta}_1) + \beta_1 + \sum_{k=1}^{M} a_{1,k}\, r(\vec{x}_j - \vec{c}_k + \vec{\delta}_1) \Big) - d_{1,i} \right]^2 \\
+ & \sum_{i=1}^{N} \frac{1}{\sigma_{2,i}^2} \left[\sum_{j=1}^{N} s_{2,ij} \Big(\alpha_2 h(\vec{x}_j + \vec{\delta}_2) + \beta_2 + \sum_{k=1}^{M} a_{2,k}\, r(\vec{x}_j - \vec{c}_k + \vec{\delta}_2) \Big) - d_{2,i} \right]^2 \\
& \;\;\vdots \\
+ & \sum_{i=1}^{N} \frac{1}{\sigma_{n,i}^2} \left[\sum_{j=1}^{N} s_{n,ij} \Big(\alpha_n h(\vec{x}_j + \vec{\delta}_n) + \beta_n + \sum_{k=1}^{M} a_{n,k}\, r(\vec{x}_j - \vec{c}_k + \vec{\delta}_n) \Big) - d_{n,i} \right]^2 \\
+ & \;\lambda \sum_{i=1}^{N} \left[h_i - \sum_{j=1}^{N} r_{ij} h_j \right]^2 .
\end{aligned}
\tag{2.44}
$$

Each one of the n first terms is related to a particular image while the last one is the smoothing term. $d_{i,j}$ is the value of the observed data in pixel j for the ith image, $\sigma_{i,j}$ its standard deviation and $s_{i,j}$ the value of PSF in the same pixel and for the same frame. We can notice that three new parameters are introduced: α, β and $\vec{\delta}$. The first one, α, is the multiplicative factor of the background: it corrects possible effects from differences in exposure times or in the transparency of the atmosphere in the case of ground-based observations, but also imposes the extended structures to have the exact same shape in each frame. The second new parameter, β, is an additive term introduced in order to get rid of errors that could have occurred during the

reduction of the images in the sky-subtraction. In this equation no constraint is applied to the intensities a of the sources: they are free to vary from one image to the other. In the case of non-varying intensities, a is multiplied by the factor α so that the images have the same ratio between the intensities of the sources and the background. The last parameter, $\vec{\delta}$, is introduced to take into account a spatial offset between two different exposures[13]. This technique is called *dithering* and is highly recommended to get rid of bad pixels and cosmic rays. Let us insist on the fact that it is preferable to deconvolve simultaneously many dithered images than one combined frame. This method is particularly well-suited to detect underlying and relatively faint structures such as lensing galaxies or Einstein rings as explained in Courbin, Lidman & Magain (1998).

A de Vaucouleurs or an exponential profile can also be used to fit a galactic light distribution in a simultaneous deconvolution. It is considered as a part of the background so it depends on the parameters α, β and $\vec{\delta}$.

Let us now conclude this section in stating the advantages of the MCS algorithm:

- This algorithm is capable of improving the resolution but also the sampling. Let us insist on the fact that this does not replace a good sampling of the original data;

- It can be applied to a single frame or to several images of the same field;

- It separates the diffuse background from the point sources without contamination;

- It calculates the position and intensity of point sources from approximate values;

- It does not need the positivity constraint to obtain good results;

- The user is guided by the value of the χ^2 and the residual maps to choose a value for the smoothing parameter and to reach the best solution.

Determination of the PSF

To optimally use the MCS algorithm, it is necessary to know the PSF $\mathcal{S}(\vec{x})$ with a great accuracy. Indeed, it is the most important point to insure that MCS will be successful.

---

[13]Practically the first image of the data set is considered as the reference frame: $\alpha_1 = 1$, $\beta_1 = 0$ and $\delta_1 = 0$.

In this work we want to treat HST/NICMOS-2 images. The Tiny Tim software package (Krist & Hook, 2004) allows the generation of HST PSFs for each instrument, filter and observing configuration. Moreover, it depends on the spectral type of the observed object. Most of the astrophysicists are usually satisfied with this PSF to get rid of the instrumental shape. But the actual PSF always departs significantly from this approximate version. And to reach the best results, we must use a better approximation. For that purpose, an algorithm was developed on the same basis as MCS to fit the PSF on one or several point sources of an image. So we can write the partial PSF $\mathcal{S}(\vec{x})$ as a sum of a function constructed on the basis of the Tiny Tim software that we call $\mathcal{P}(\vec{x})$ plus a numerical background that we call $\mathcal{B}(\vec{x})$ and which is determined by comparison with actual point source images in the frame:

$$\mathcal{S}(\vec{x}) = \mathcal{P}(\vec{x}) + \mathcal{B}(\vec{x}). \tag{2.45}$$

Let us notice that the total PSF $\mathcal{T}(\vec{x})$ can also be written that way because it has the same shape as $\mathcal{S}(\vec{x})$.

If we consider a single frame, the function to minimize is the same as Eq. 2.33 where $\mathcal{D}(\vec{x})$ is replaced by $\mathcal{T}(\vec{x})$ and $\mathcal{S}(\vec{x})$ is replaced by $\mathcal{R}(\vec{x})$ in order to construct $\mathcal{S}(\vec{x})$. It gives, for a one-dimensional image with a point source centered in c and with the usual notations:

$$
\begin{aligned}
\mathcal{K}_\mathcal{S} \;=\; & \sum_{i=1}^{N} \frac{1}{\sigma_i^2} \Big[\sum_{j=1}^{N} r_{ij} \Big(p(x-c) + b(x-c) \Big)_j - t_i \Big]^2 \\
& + \; \lambda \sum_{i=1}^{N} \Big[f_i - \sum_{j=1}^{N} w_{ij} f_j \Big]^2
\end{aligned}
\tag{2.46}
$$

where w_{ij} represents a length scale for the smoothing term. Practically, we choose w_{ij} equal to r_{ij} because, if a deconvolved frame cannot contain any frequency higher than $\mathcal{R}(\vec{x})$, then neither should the PSF $\mathcal{S}(\vec{x})$ used for its construction. The parameters to modify during the iterations of the algorithm are the following: the center of the point source, its intensity and all the pixels b_i from the numerical background image.

Let us not forget that the MCS algorithm allows the user to oversample the deconvolved frame compared to the original data. This is mainly useful if we have several images of the same field with the object position shifted on the detector. But it also requires the instrumental profile itself to be oversampled by the desired factor. To do so we take advantage of the presence of several point sources on one frame: they are located on different places on the CCD, so they can be deconvolved at the same time, each one of them

constraining the numerical background of the unique oversampled output PSF. That gives a PSF with a higher S/N than in one fit on a single source.

Checking the residual maps allows the user to possibly detect a variation of the PSF in the field or a contamination by an underlying or neighboring object that is not obvious on the original frame.

More recently, Magain et al. (2007) presented a method, derived from MCS, to determine the PSF on images consisting of possibly blended point sources. This method works well, even in very crowded fields, when no point source is sufficiently isolated to derive an accurate PSF from standard techniques.

The next section presents a method which extends the one of Magain et al. (2007) to images containing a mixture of point sources and diffuse background. It is based on an iterative scheme, in which both the PSF and diffuse background are improved step by step.

Chapter 3

The iterative method using the MCS algorithm

We developed an iterative procedure using the MCS algorithm to treat archival HST/NICMOS-2 (Noll et al., 2004; Dickinson et al., 2002) images of gravitationally-lensed quasars.

Unfortunately, for the gravitational mirages that are of interest to us, no extra images of stars are available to improve the PSF: we have to use the information in the point sources of the lensed system itself. However, we know there may be some extra structure under the point sources, as well as a contribution from the lensing galaxy. The difficulty resides in the separation of these contributions from the point sources themselves.

The originality of the present method is that the same images are used to determine the PSF and to perform the deconvolution (basically to detect the diffuse background and to obtain the astrometry and photometry of all objects). It works only if there are several point sources in the field: this makes it possible to distinguish the structures belonging to the PSF, and thus appearing in the vicinity of each point source, from the diffuse background assumed not to be identical around each source.

This new method is based on an iterative procedure. We start with a first approximation of the PSF, in the case of HST images this PSF is constructed by the Tiny Tim software (Krist & Hook, 2004; see Fig. 3.1 for an example of a Tiny Tim PSF), with a sampling step two times smaller than the original one (oversampling of a factor of two). That instrumental profile is deconvolved by the final Gaussian PSF $\mathcal{R}(\vec{x})$ in order to obtain the deconvolution kernel that we call $\mathcal{S}_0(\vec{x})$. This is a reasonable first approximation,
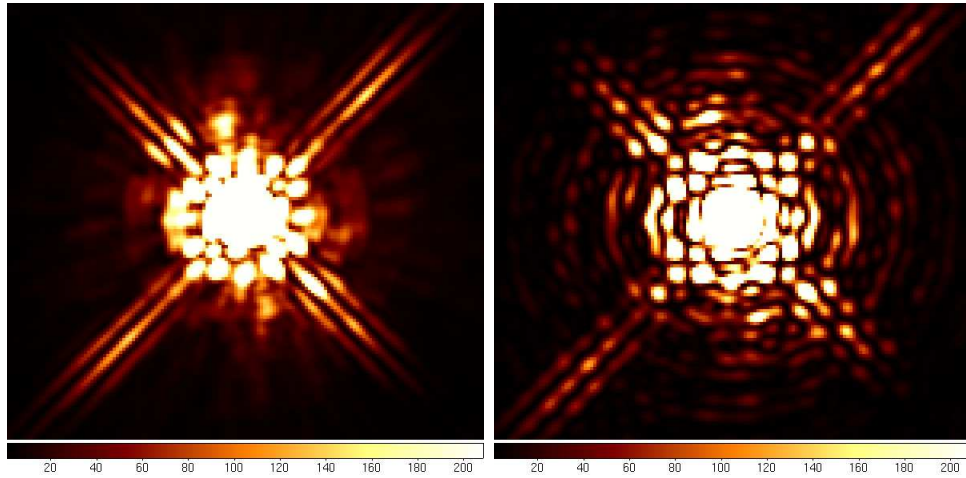
Figure 3.1: PSF constructed by the Tiny Tim software for two filters available on NIC-2. They are considerably different. However we can easily notice that they both have complex structures including spikes. *Left*: a PSF for the F160W filter (defined in the next chapter). The colour scale goes from 0% (black) to 0.13% (white) of the peak intensity. *Right*: a PSF for the F180M filter (defined in the next chapter). The coulour scale goes from 0% (black) to 0.16% (white) of the peak intensity.

although not accurate enough to obtain trustworthy deconvolved frames. Indeed, when using that instrumental profile for deconvolving original images, which we call $\mathcal{D}_0(\vec{x})$, significant structures appear around each point source, clearly showing that the Tiny Tim PSF departs from the actual one. An example is shown on Fig. 3.2: it is the simultaneous deconvolution of four frames of the Cloverleaf gravitational lens[1] through the F160W filter.

For all these reasons we proceed as follows:

1. First, for each individual image, we determine an improved PSF following the method described in Magain et al. (2007). This is done by adding a numerical background to the approximate PSF $\mathcal{S}_0(\vec{x})$ (here, the deconvolved Tiny Tim PSF) so that the observed image $\mathcal{D}_0(\vec{x})$ is reproduced better. But, since this method assumes that the image contains only point sources, and since our object is supposed to contain a diffuse component, a part of it will be wrongly included in the improved PSF $\mathcal{S}_1(\vec{x})$. If the structures of the diffuse component were identical around each point source, it would be entirely included in the PSF. On the other hand, assuming that the quasar is quadruply-

---

[1]See section 4.1 for details on this object.
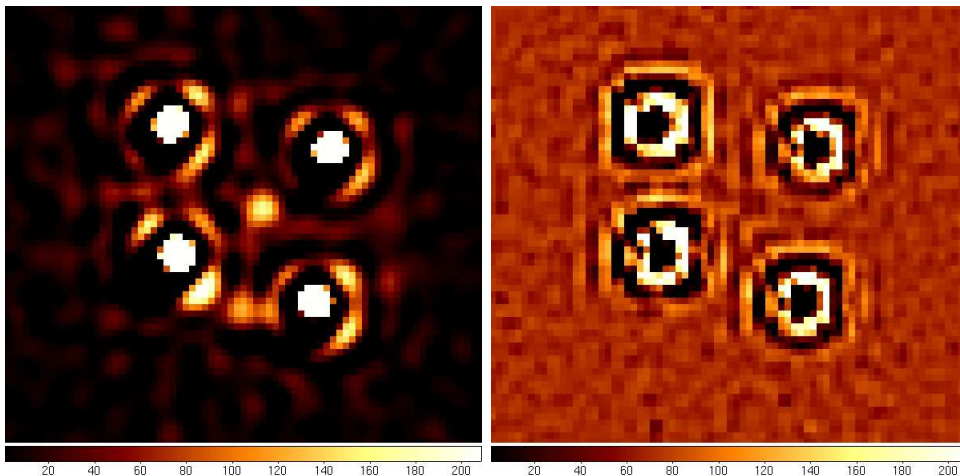
Figure 3.2: Results of the simultaneous deconvolution of a quadruply-lensed quasar, the *Cloverleaf*, using a Tiny Tim PSF. *Left*: deconvolved image, the colour scale going from 0% (black) to 0.4% (white) of the maximum intensity. *Right*: residual map of the deconvolution. The remnant structure around each point source is obvious and is due to the use of an inaccurate PSF.

lensed, and if the background were completely different around each of the point sources, only around 25% of it would be included in the PSF. In practice, a variable fraction of the background goes into the PSF. As long as that fraction is below 100%, our iterative procedure will allow improvements of the results.

2. We then use the once-improved PSFs $\mathcal{S}_1(\vec{x})$ to perform a simultaneous deconvolution of all images. Let us insist on the fact that each image has its own instrumental profile: $\mathcal{S}_1(\vec{x})$ varies slightly from image to image. The simultaneous deconvolution allows us to obtain a first approximation of the diffuse background, $\mathcal{H}_1(\vec{x})$, which, by construction, is the same in each image. However, since a part of the actual background was included in the PSFs $\mathcal{S}_1(\vec{x})$, $\mathcal{H}_1(\vec{x})$ is only the remaining part of the actual background.

3. We subtract $\mathcal{H}_1(\vec{x})$, reconvolved and resampled to the initial resolution, from the original images. This gives us a new version of the observed images, $\mathcal{D}_1(\vec{x})$, containing a lower amount of diffuse background. The first iteration is over.

4. To begin the second iteration, we use the images $\mathcal{D}_1(\vec{x})$ to determine

the PSFs $\mathcal{S}_2(\vec{x})$. As $\mathcal{D}_1(\vec{x})$ contains a lower amount of background than $\mathcal{D}_0(\vec{x})$, the new PSFs are indeed closer to the correct ones.

5. The simultaneous deconvolution of the original images $\mathcal{D}_0(\vec{x})$ with the new PSFs $\mathcal{S}_2(\vec{x})$ allows us to get a diffuse background $\mathcal{H}_2(\vec{x})$ which is improved with respect to the one obtained at the previous iteration.

6. We subtract $\mathcal{H}_2(\vec{x})$ from the original images $\mathcal{D}_0(\vec{x})$. This closes the second iteration.

7. The iterative procedure is continued until no significant improvement is observed. Usually around 3 to 5 iterations are necessary, depending on the structures under the sources.

This iterative process is illustrated on real examples in the next chapter. Sometimes this process needs to be adapted to the case treated. For example when the diffuse background is not faint enough comparing to the intensities of the sources, it is better to first deconvolve simultaneously the data with the Tiny Tim PSFs than to start in fitting these PSFs on the point sources. Indeed, these latter sources are strongly contaminated by the intense extended structures such as an obvious lensing galaxy. Before subtracting the background obtained thanks to the Tiny Tim PSFs from the original images, it is necessary to clean it from the bad structures which are created to compensate the inaccuracies in the Tiny Tim PSFs. This demands some intuition to decide what is part of the real background and what is not. At this stage it is always better to remove too many structures than too few because it is possible to recover them in the next iterations.

Chapter 4

Applications

Contents

4.1 The Cloverleaf (H1413+117)

4.1.1 Introduction

Four years after its discovery in 1984 by Hazard et al., the QSO H1413+117 was identified as a gravitational lens by Magain et al. (1988). This system, consisting in 4 components of comparable brightness separated by ~ 1 arcsec, is best known as the *Cloverleaf*. It is also one of the brightest quasars amongst the BAL (Broad Absorption Line) class, with a redshift of 2.558 and an apparent visual magnitude of 17. The lensing galaxy was detected by Kneib, Alloin & Pello (1998) from a careful PSF subtraction on near-infrared HST images. Let us try to apply our iterative method on this set of images and on another one which was taken with a different filter. We will see that it permits to obtain a more accurate astrometry of the system and a better characterization of the lensing galaxy. Moreover, it will also allow the detection of additional structures, such as parts of an Einstein ring. All these facts are also related in an article presented in appendix.

4.1.2 HST imaging

The first set of HST data (PI: E. Falco) was obtained on the 28th of December 1997 by the camera 2 of NICMOS[1] with the F160W filter, a wide band filter corresponding approximately to the near-IR H-Band. We use the four calibrated images, i.e. treated by CALNICA, the HST image reduction pipeline. Each of them has an exposure time of 639.9389 s and a mean pixel size of $0''.07510$ according to the version 6.3 of the Tiny Tim software (Krist & Hook, 2004). These images were obtained in the MULTIACCUM mode: each of them is a combination of several samples, 19 in the present case. A combination of these four images is shown on the left panel of Fig. 4.1.

The second set of frames (PI: D. A. Turnshek) was obtained on the 10th of July 2003 with the same instrument in the F180M medium-band filter. As for the F160W filter we use the calibrated images, here eight frames, four of them being a combination of 18 samples and the other four being a combination of 16 samples. The first four have an exposure time of 575.9418 s and the latter four an exposure time of 447.9474 s. The mean pixel size is, again according to the Tiny Tim software (Krist & Hook, 2004), $0''.07568$. A combination of these calibrated images is shown on the right panel of Fig. 4.1.

---

[1]Let us recall that NICMOS stands for Near Infrared Camera and Multi-Object Spectrometer
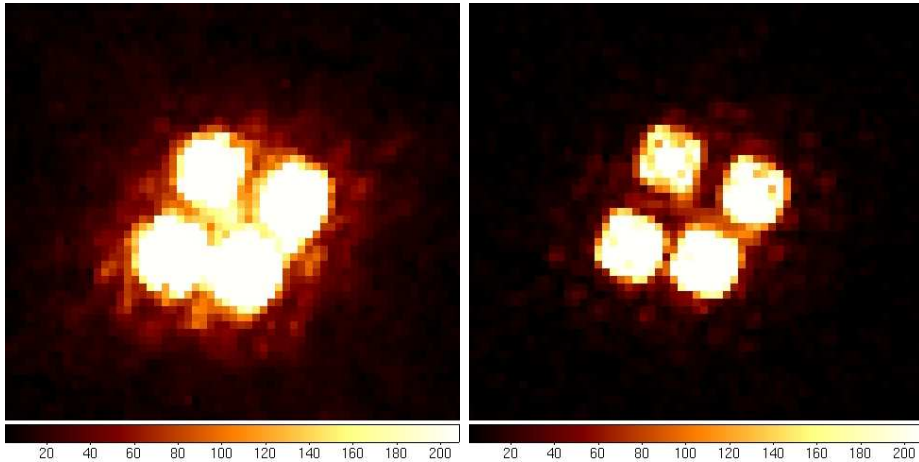
Figure 4.1: Combined HST/NICMOS-2 images of the Cloverleaf. *Left*: combination of the 4 calibrated and reduced images obtained with through the F160W filter. The colour scale goes from 0% (black) to 2.4% (white) of the maximum intensity. *Right*: combination of the 8 calibrated and reduced images obtained with through the F180M filter. The colour scale goes from 0% (black) to 5% (white) of the maximum intensity. The structure of the PSF is noticeable. North is to the top and East to the left.

The wavelength ranges of these two filters are partly superimposed: the passband of the F160W filter is 1.4 $\mu m \leq \lambda \leq$ 1.8 μm while it corresponds to 1.76 $\mu m \leq \lambda \leq$ 1.83 μm for the F180M filter. The latter was chosen in order to include the oxygen [OIII] forbidden line doublet (499 – 501 nm) at the redshift of the QSO.

The image reduction was divided into two parts: the image cleaning and the calculation of the sigma images, i.e. the frames containing the standard deviations of the pixel intensities. The first step of the first part consists in computing the intensities in counts per pixel. The second step consists in removing the sky background, which is mostly caused by the zodiacal light[2] at short wavelengths and by the thermal emission from the telescope at long wavelengths. As the NIC-2 detector is composed of four quadrants, it is necessary to subtract a different constant value for each of them. These constants were derived from the parts of the image where no obvious light source is observed.

The second step consists in the calculation of the sigma images. We start from the sigmas obtained by the pipeline CALNICA. Two effects are then corrected. First, we take into account the underevaluation of the standard

---

[2]See definition in the glossary, page 83.

deviation for the negative pixels: we replace all negative intensities by a null value. Secondly, we make use of the HST flag files indicating bad pixels, e.g. cold or hot pixels. It allows us, using the inverted sigma images, to put the statistical weight of such bad pixels to zero so that the information they provide has no influence on the deconvolution.

Let us mention that, at the time of these tests, we did not remove the cosmic ray impacts from the images during the reduction process. We used the deconvolution residuals (see section 2.3.3) to spot the pixels having been likely contaminated by a cosmic ray. We then put the inverted sigma value of such pixels to zero.

All the manipulations are carried out with the IRAF[3] package.

4.1.3   Deconvolution

The iterative method is then applied to both sets of reduced images in order to improve their resolution and sampling and, most importantly, to detect any significant extended structure which might be hidden by the complex PSF. In order to improve the resolution while keeping a well sampled light distribution, we use a sampling step 2 times smaller than the original pixel size and we choose, as the final PSF $\mathcal{R}(\vec{x})$, a Gaussian with a FWHM of 2 pixels in the new sampling grid[4]. Let us mention that, since the HST PSF varies with the position in the focal plane, and since the object is located in different parts of the detector at each exposure, each original image has its own individual PSF.

For the F160W data set, seven iterations are necessary while, for the F180M data set, convergence is reached after three iterations. This difference is due to the fact that the diffuse background is less intense relative to the point sources in the latter filter. Fig. 4.2 and 4.3 illustrate the evolution of the PSF in the iterative scheme: they show the corrections applied at different stages. We can see that the first step of the iterative process changes significantly the PSF obtained with Tiny Tim. The next steps allow smaller adjustments and smaller details. In the case of the F180M filter, it is obvious that only 3 iterations are necessary, as the corrections already become negligible after the second step. The same happens after the sixth iteration in the F160W filter.

---

[3]IRAF, Image Reduction and Analysis Facility, is distributed by the National Optical Astronomy Observatories, which are operated by AURA, the Association of Universities for Research in Astronomy, Inc., under cooperative agreement with the NSF, National Science Foundation.

[4]2 pixels in the new grid correspond to 4 pixels in the original frame.
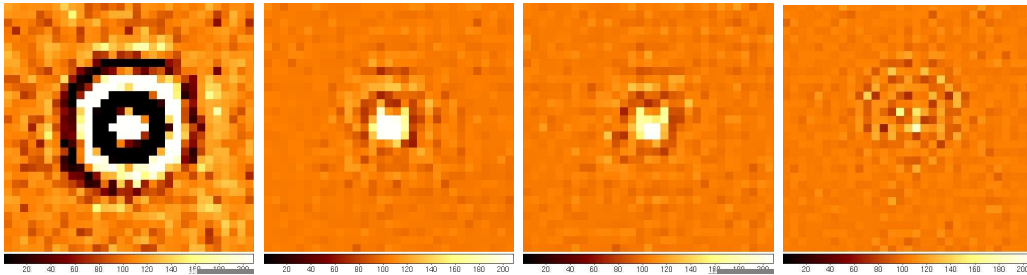
Figure 4.2: Corrections applied to the PSFs for one image of the F160W data set at different stages of the process. The colour scale goes from -1.3% (black) to +1.3% (white) of the peak intensity of the Tiny Tim PSF. *Left*: corrections to the PSF at the first iteration, starting from the deconvolved Tiny Tim PSF. *Middle left*: corrections at the second iteration. *Middle right*: corrections at the fourth iteration. *Right*: corrections at the last iteration.
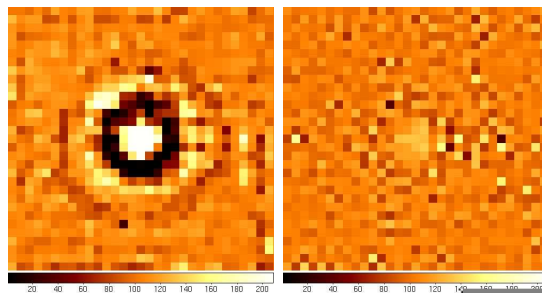
Figure 4.3: Corrections applied to the PSFs for one image of the F180M data set at different stages of the process. The colour scale goes from -4.8% (black) to +4.8% (white) of the peak intensity of the Tiny Tim PSF. *Left*: corrections to the PSF at the first iteration, starting from the deconvolved Tiny Tim PSF. *Right*: corrections at the last iteration.

Now that we have an idea about the evolution of the successive corrections applied to obtain a trustworthy instrumental profile, we can focus on the results of the deconvolution itself. Fig. 4.4 and 4.5 show the deconvolved frames from the last iteration, respectively for the F160W and the F180M data set. A partial Einstein ring, which is the gravitationally-lensed image of the quasar host galaxy, and the lensing object can be seen for both sets on the background frame (top right) and on the background plus point sources frame (top left). The lens galaxy appears less intense compared to the point sources in the F180M filter, which is expected as it is a medium-band filter including the [OIII] emission lines (499 – 501 nm) at the redshift of the QSO, but no emission line at the redshift of the lens. The partial Einstein
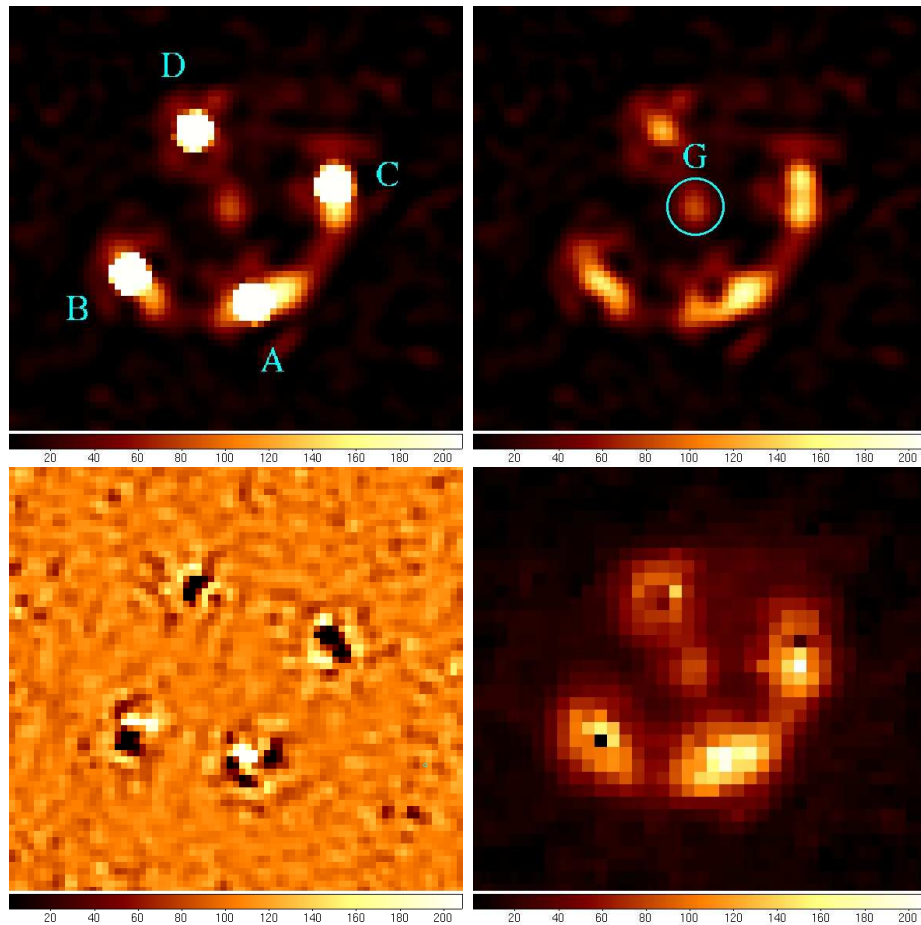
Figure 4.4: Results of the last simultaneous deconvolution for the F160W data set. North is to the top and East to the left. *Top left*: deconvolved image, i.e. point sources plus smooth background; the point sources are labeled as in Magain et al. (1988). *Top right*: smooth background common to all images of the set where the lensing galaxy G is encircled. *Bottom left*: mean residual map of the simultaneous deconvolution. *Bottom right*: image reconvolved to the instrument resolution and sampling, with the point sources removed.

ring also has a different structure: compared to the F160W filter, it appears more intense in the F180M filter close to the point sources and less intense in between them. This suggests that the NLR[5] is more compact than the global lens galaxy, which could have been expected.

The residual map (see bottom left panel of Fig. 4.4 and 4.5) guides us

---

[5]To learn more about the NLR, see section 2.1.3.
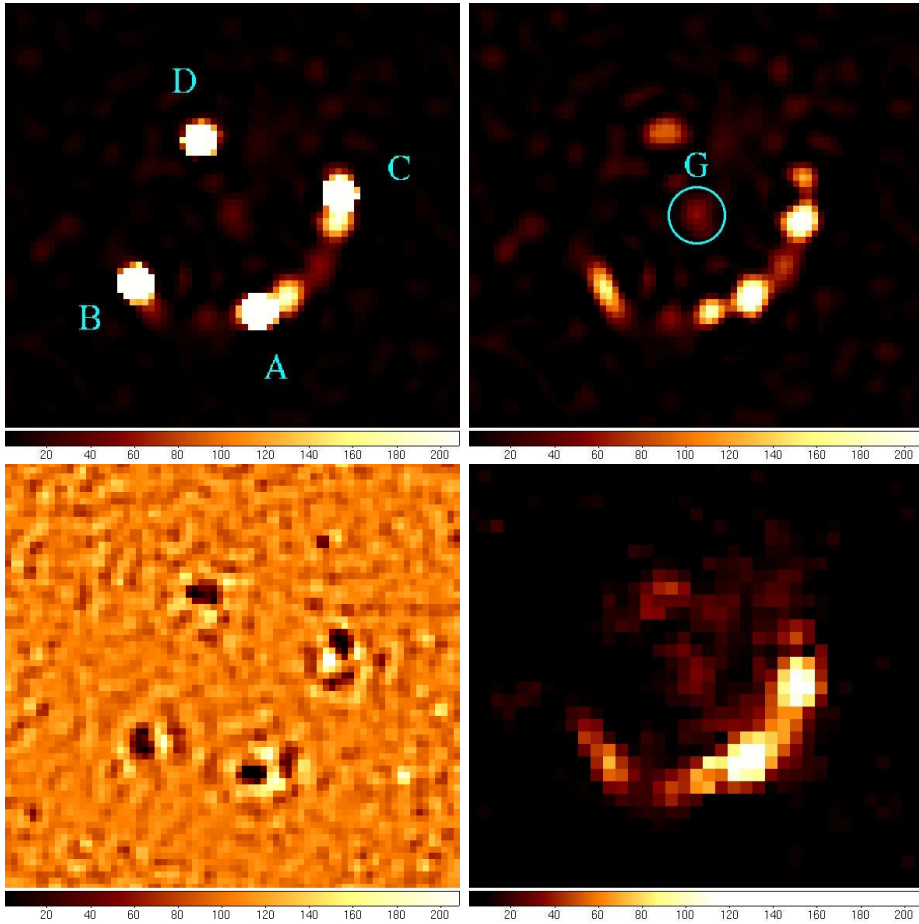
Figure 4.5: Results of the last simultaneous deconvolution for the F180M data set. North is to the top and East to the left. *Top left*: deconvolved image, i.e. point sources plus smooth background; the point sources are labeled as in Magain et al. (1988). *Top right*: smooth background common to all images of the set where the lensing galaxy G is encircled. *Bottom left*: mean residual map of the simultaneous deconvolution. *Bottom right*: image reconvolved to the instrument resolution and sampling, with the point sources removed.

through the different steps of the iterative process. We can see that, for both sets at the last iteration, there is some structure left under the point sources, but nothing systematic, and there is nearly no remnant structure where the ring and the lensing galaxy are located. The fact that the residuals under the four point sources have very different shapes suggests that they are not due to errors in our instrumental profile, but rather to small PSF variations from one QSO image to the other.

We calculate the reduced chi square χ_r^2 for each set and each iteration step in the zone of interest, i.e. in a square containing the four point sources and the extended structures (ring plus lens). In the last iterations it barely changes: the PSF is not improved significantly anymore and the iterative process has converged. We obtain a χ_r^2 of 3.845 for the F160W data set after the seventh iteration, and a χ_r^2 of 1.125 for the F180M data set after the third iteration, which is really good. Let us mention that these values are computed taking into account all images of a given set, so that any slight incompatibility between some of the input images results in an increase of the χ^2 that cannot be lowered by changing the model. A final χ_r^2 of 1 means that the model is perfectly compatible with all the images of the set. It implies that all the images are statistically compatible with each other and that the PSF is perfectly known. Any inaccuracy in the data acquisition or reduction will also increase the final χ^2.

4.1.4   Astrometry and photometry

Tables 4.1 and 4.2 give the relative astrometry and photometry for the quasar images as well as for the lens, in the F160W filter and the F180M filter respectively. The coordinates are measured in arcsec relative to component A (see Figs. 4.4 and 4.5). The apparent magnitudes are given in the Vega system.

As the geometric distortions for the HST/NIC-2 depend on the position on the CCD, their proper corrections require an individual deconvolution of each image. We obtain the position of each point source, relative to source A, on each individually deconvolved frame and we correct them from the

Table 4.1: Relative astrometric and photometric measurements for the four components and lensing galaxy of the Cloverleaf, in the F160W filter. The right ascension α and the declination δ are given in arcsecond relative to component A. The photometry is given in apparent magnitude in the Vega system. The internal 1σ error bars are also indicated.

| ID | F160W | | |
	$\Delta\alpha$ (″)	$\Delta\delta$ (″)	Magnitude
A	0.	0.	15.760 ± 0.002
B	0.7426 ± 0.0002	0.1686 ± 0.0004	15.863 ± 0.005
C	-0.4930 ± 0.0003	0.7135 ± 0.0004	16.143 ± 0.004
D	0.3526 ± 0.0007	1.0394 ± 0.0004	16.400 ± 0.006
G	0.1365 ± 0.0024	0.5887 ± 0.0035	20.527 ± 0.037

Table 4.2: Relative astrometric and photometric measurements for the four components and lensing galaxy of the Cloverleaf, in the F180M filter. The right ascension α and the declination δ are given in arcsecond relative to component A. The photometry is given in apparent magnitude in the Vega system. The internal 1σ error bars are also indicated.

ID	F180M		
	$\Delta\alpha$ ($''$)	$\Delta\delta$ ($''$)	Magnitude
A	0.	0.	15.548 ± 0.006
B	0.7458 ± 0.0003	0.1688 ± 0.0002	15.650 ± 0.009
C	-0.4917 ± 0.0003	0.7105 ± 0.0003	15.902 ± 0.004
D	0.3532 ± 0.0003	1.0400 ± 0.0002	16.218 ± 0.007
G	0.1255 ± 0.0036	0.6192 ± 0.0069	22.182 ± 0.101

distortions according to the formulae given in the NICMOS Data Handbook (Noll et al., 2004). We can then compute average values. For the point sources, this gives more accurate results than a simultaneous deconvolution with a mean correction on the coordinates. On the other hand, this is not true for the lensing galaxy and the Einstein ring. As these objects are faint, it is better to rely on the results of the simultaneous deconvolution, where the signal in the whole set of images is used to constrain their shape. A mean geometric correction can be applied, whose internal errors are lower than the random uncertainties on these faint components.

The error bars given in Tables 4.1 and 4.2 are internal errors. The listed values are the standard deviation of the mean computed from the individual deconvolutions.

The astrometric precision for the point sources is about 0.5 milliarcsec in the F160W filter and 0.3 milliarcsec in the F180M filter. The higher precision in the medium-band filter may be explained by the fact that the partial ring and the lens galaxy appear fainter relative to the point sources and thus have a lower contribution to the error bars.

Of course, the precision on the position of the lens galaxy is significantly lower. This is due to the facts that (1) it is a diffuse object, (2) it is much fainter than the point sources (about 4.5 mag in the F160W filter and 6.4 mag in the F180M filter) and (3) it is mixed with the PSF wings of the point sources.

Tables 4.1 and 4.2 also show that the results derived from both filters are not compatible within their internal error bars. As the geometry of the system is not expected to vary on the time scale of a few years, this disagreement suggests that the actual error bars are significantly larger than

the internal ones. The causes may be diverse. As the two sets of data were acquired six years apart, with a different orientation of the HST and thus of the detector, and in different cycles of NICMOS (pre- and post-NCS, NICMOS Cooling System[6]), some geometrical distortions may not have been completely taken into account. The uncertainties concerning the coefficients of the formulae used to correct for the geometrical distortions, as given in the NICMOS Data Handbook (Noll et al., 2004), account for an uncertainty of the order of 0.1 milliarcsec in each filter, which is about an order of magnitude smaller than the external errors we obtain (see next paragraph). It is thus possible that a residual distortion of the NICMOS images remains, at the 10^{-3} level of accuracy, i.e. 0.001 arcsec per arcsec. An imperfect separation of the partial Einstein ring from the point sources in the deconvolution process as well as some inaccuracies in the PSF recovery may also play a role.

The external errors, computed by comparing the source positions derived from the two data sets, are the following: the average difference in position between the point sources amounts to 1.4 milliarcsec. Assuming that the errors in both data sets contribute equally to this difference, we derive a value of $1.4/\sqrt{2} \approx 1$ milliarcsec (i.e. 0.013 pixel) for the estimated accuracy in the position of the point sources.

Our measurements are compared to those of Magain et al. (1988) and Turnshek et al. (1997) given in Table 4.3. The latter were derived from images acquired with other HST instruments, the Wide Field Planetary Camera and the Wide Field Planetary Camera 2, and with a completely different image processing technique, while the first ones were obtained from much lower resolution ground-based images. For both sets of results we indicate the 1σ error bars. Let us mention that they do not appear in the original paper of Magain et al. (1988). The average difference between our results and those of Magain et al. (1988) amounts to 4 milliarcsec, which is close to the error bars on the measurements performed by these authors. The same comparison with Turnshek et al. (1997) gives an average difference of 2.6 milliarcsec, also compatible with their error bars.

The primary lens, a single galaxy, was detected in 1998 by Kneib et al. After a PSF subtraction of the four lensed images they obtained the following relative position for the lensing galaxy:

$$\alpha \;=\; 0.112'' \;\pm\; 0.02''$$

and

$$\delta \;=\; 0.503'' \;\pm\; 0.02''$$

---

[6]The instrument ran out of nitrogen coolant sooner than expected in January 1999. During a Hubble Service Mission in 2002, a cryocooler was installed on board the HST: it now cools NICMOS through a cryogenic (below 123 K) neon loop.

Table 4.3: Relative astrometry of the Cloverleaf from Magain et al. (1988) and from Turnshek et al. (1997). The right ascension α and the declination δ are given in arcsecond relative to component A. The 1σ error bars are also indicated.

ID	Magain et al. (1988)		Turnshek et al. (1997)	
	$\Delta\alpha$ ($''$)	$\Delta\delta$ ($''$)	$\Delta\alpha$ ($''$)	$\Delta\delta$ ($''$)
A	0.	0.	0.	0.
B	0.753 ± 0.006	0.173 ± 0.006	0.744 ± 0.003	0.172 ± 0.003
C	-0.496 ± 0.004	0.713 ± 0.003	-0.491 ± 0.003	0.716 ± 0.004
D	0.354 ± 0.004	1.043 ± 0.004	0.355 ± 0.003	1.043 ± 0.012

This result is compatible with ours in right ascension: $\Delta\alpha = -0.025''\pm0.020''$. But this is not true for the declination: $\Delta\delta = -0.086'' \pm 0.020''$. Possible systematic errors, in particular on the lens position, are investigated in the next section.

Finally, as already mentioned, the intensity distribution along the partial Einstein ring is significantly different in the two filters: it is more regular in the wide band filter, F160W, than in the narrower one, F180M. As the latter was chosen to emphasize the [OIII] emission lines (499 – 501 nm) and thus to obtain a mapping of the narrow emission line region in the quasar host galaxy, such a difference is not unexpected. The partial ring observed in the broad-band filter is a distorted image of the full host galaxy, while the narrow emission-line region is more prominent in the F180M filter. In particular, two bright knots are seen close to the A and C images of the quasar (see Fig. 4.5). These knots cannot correspond to deconvolution artifacts, which might be caused, e.g., by an imperfect modeling of the PSF. Indeed, such artifacts would be expected around all point sources and at the same position relative to these point sources, which is not the case. Moreover, the observed positions are in agreement with the inverted parity expected between two neighboring images in such a lensed system. These bright knots must therefore correspond to the emission line region in the quasar host galaxy, which is thus probably brighter on one side than on the other. A detailed modeling of the system, including an inversion of the lens equation, should allow the reconstruction of an image of the host galaxy and of the narrow line region. This would be the first time one could map the host and narrow line region of a BAL QSO at such a high redshift.

4.1.5   Synthetic image

The accuracy of our results is further tested by carrying the same procedure on a synthetic image having characteristics similar to those of the HST/NIC-2 F160W images of the Cloverleaf: 4 point sources, a faint lensing object and a partial Einstein ring (see left frame of Fig. 4.6). This synthetic image was convolved with a PSF similar to the actual one, but unknown to the test performer. Random noise was then added to get a S/N comparable to that of the combined HST image (see right frame of Fig. 4.6). The results
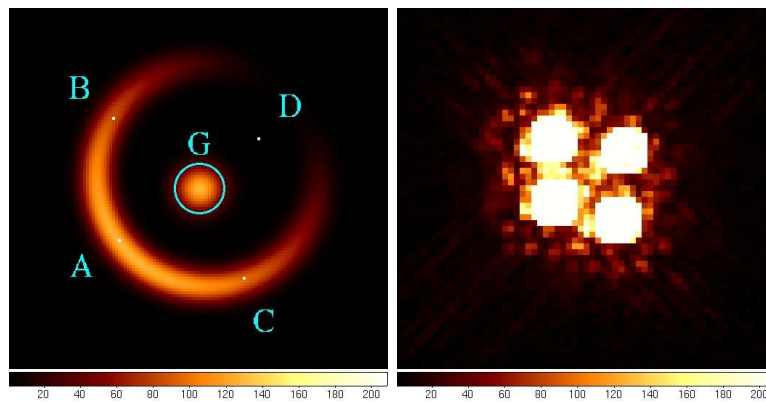
Figure 4.6: *Left*: synthetic image of a gravitationally-lensed quasar with a configuration similar to the Cloverleaf: 4 point sources, a faint lensing object, and a partial Einstein ring. The orientation is the same as in the original F160W Cloverleaf images. *Right*: the same image convolved with a HST-type PSF unknown to the test performer and with random noise similar to the actual observations.

obtained after three iterations are presented on Fig. 4.7, which displays the background, the point sources plus background and the residual map. Some remnant structures can be seen under the point sources on the residual map. The residuals are slightly weaker than those observed in the residual maps of the actual images, but show similar characteristics.

On average, the flux in the background (ring + lens) is recovered within 4% , which can be considered as excellent since this diffuse background is very weak compared to the point sources. However, because of the smoothing constraint, the deconvolved ring and lens appear slightly flatter than the original ones. The largest differences are found under the brightest point source (A), where the deconvolved ring is about 43% below the original one.

Table 4.4 summarizes the astrometry carried out on this artificial Clover-
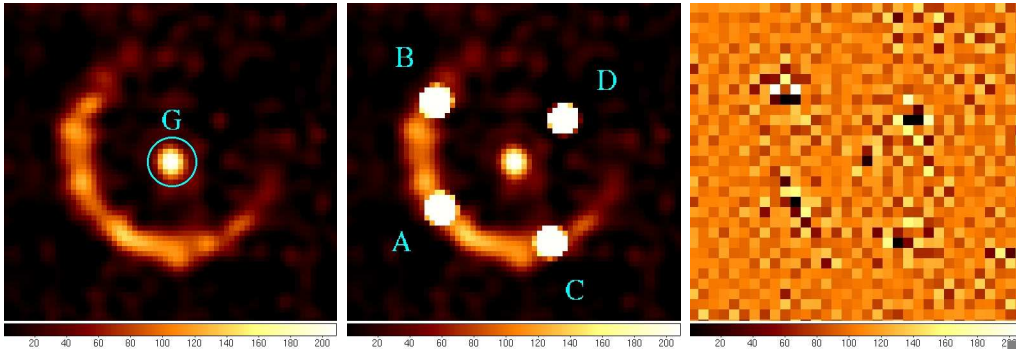
Figure 4.7: Results of the last iteration on the synthetic image. *Left*: diffuse background. *Middle*: diffuse background plus point sources. *Right*: residual map of the deconvolution.

leaf: the first pair of columns present the measurements made on the final deconvolved image resulting from the iterative process, the second pair of columns the results when using a deconvolved Tiny Tim PSF for a unique deconvolution, and the last one the measurements made on the original image.

The differences between the positions obtained for a particular source reach a maximum of about 0.3 milliarcsec with a mean value around 0.1 milliarcsec, which is slightly better than the internal precision estimated in Tables 4.1 and 4.2 and significantly more accurate than the ones obtained from the deconvolution with the Tiny Tim PSF. On the other hand, the lens galaxy position is not as accurate as the ones of the point sources: the maximum difference amounts to 20 milliarcsec (i.e. a quarter of a pixel). Indeed, the position of such very faint diffuse objects is rather sensitive to inaccuracies in the PSF: any error in the wings of a bright point source PSF may have impacts on the faint neighboring objects.

Table 4.4: Relative astrometry of the artificial Cloverleaf. The two coordinates are given in arcsecond relative to component A.

ID	Iterative process $\Delta\alpha$ ($''$)	$\Delta\delta$ ($''$)	Tiny Tim $\Delta\alpha$ ($''$)	$\Delta\delta$ ($''$)	Original image $\Delta\alpha$ ($''$)	$\Delta\delta$ ($''$)
A	0.	0.	0.	0.	0.	0.
B	0.7719	0.1770	0.7726	0.1755	0.7718	0.1767
C	-0.4538	0.7140	-0.4538	0.7129	-0.4538	0.7138
D	0.3913	1.0480	0.3921	1.0483	0.3913	1.0479
G	0.1826	0.6151	0.1787	0.5877	0.1819	0.5940

Given these possible sources of errors and the results of the simulations, we estimate the accuracy on the lens galaxy position to amount to some 20 milliarcsec.

4.2   WFI J2033-4723

4.2.1   Introduction

WFI J2033-4723, a quadruply–imaged quasar, was discovered in La Silla, Chile, during an optical survey using the MPG/ESO 2.2 m telescope operated by the European Southern Observatory (ESO). This discovery is related by Morgan et al. (2004). The source redshift is 1.66 while, according to Eigenbrod et al. (2006), the galaxy has a redshift of 0.661. The magnitude of the entire system is estimated at ~ 17.9 in the g filter which passband is $458 \; nm \leq \lambda \leq 528 \; nm$. The maximum separation between two lensed images amounts to $2\overset{''}{.}5$. This gravitational mirage is surrounded by at least six galaxies within a radius of 20 arcsec, which makes it a difficult system to model.

4.2.2   HST imaging

Our set of images was acquired with camera 2 of NICMOS through the F160W filter on the 14th of April 2004. The set is composed of four images obtained in the MULTIACCUM mode: the first frame is a combination of 19 samples while the other three frames are a combination of 20 samples. As a consequence, the first image has an exposure time of 639.9389 s while the others have an exposure time of 703.9361 s. According to the version 6.3 of the Tiny Tim software (Krist & Hook, 2004), the mean pixel size of these frames is $0\overset{''}{.}07568$. As for the Cloverleaf, we use the images calibrated by CALNICA[7]. A combination of these four images is shown on Fig. 4.8. Let us notice that the lensing galaxy is already observable, in between the four point sources. Moreover, another object is present to the North of the system. It turns out to be a nearby galaxy according to Morgan et al. (2004).

The image reduction we apply is the same as for the Cloverleaf: it is described in section 4.1.2. Let us just recall that it is divided into two parts: the image cleaning and the calculation of the sigma frames which are of great importance in our deconvolution algorithm.

---

[7]Let us recall that CALNICA is the HST image reduction pipeline.
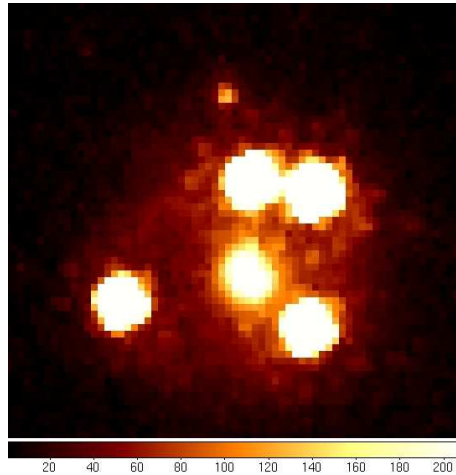
Figure 4.8: Combination of the four calibrated and reduced images of WFI J2033-4723 obtained with the F160W filter of NIC-2. The colour scale goes from 0% (black) to 2.8% (white) of the maximum intensity. North is to the top and East to the left.

4.2.3   Deconvolution

Here again, as no extra star is available, we use the iterative method which allows us to improve the Tiny Tim PSF step by step and to separate possible significant extended structures from the point sources. As in the case of H1413+117, we use a sampling step 2 times smaller than the original pixel size and a Gaussian with a FWHM of 2 pixels for $\mathcal{R}(\vec{x})$, i.e. the PSF of the deconvolved image. These choices allow an improvement of the resolution of the deconvolved frame comparing to the original images as well as a good sampling of the resulting light distribution.

Convergence is reached after three iterations and the reduced χ^2 amounts to 3.59. The results are shown on Fig. 4.9. The mean residual map shown on the right panel indicates that there is no systematic structure under the lensed images. That means that the instrumental profile is well-adapted. The irregular remnant structures are probably due to small variations of the PSF in the field.

On Fig. 4.9, the resulting deconvolved frame was obtained with a larger smoothing parameter than the one leading to the best reduced χ^2: the aim is simply to get a flatter and less noisy background. In doing so we highlight the presence of a diffuse and faint background surrounding the four lensed images (see middle panel). Several questions come straight to mind: at which distance is this structure located? It could be a kind of halo associated to the lens galaxy. But then why is it encircling the lensed images? In such a
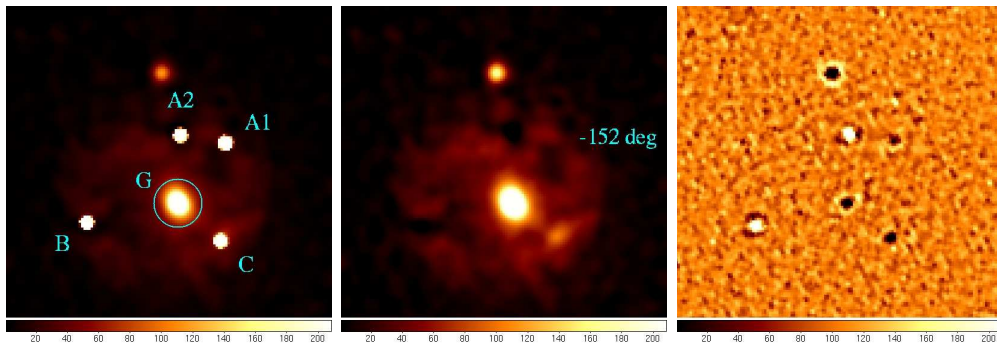
Figure 4.9: Results of the last simultaneous deconvolution for WFI J2033-4723. North is to the top and East to the left. *Left*: deconvolved frame, i.e. point sources plus smooth background; the point sources are labeled as in Morgan et al. (2004) and the lensing galaxy G is encircled. *Middle*: smooth background common to all images. *Right*: mean residual map of the simultaneous deconvolution.

case it would not be related to them. It is thus very unlikely that we are precisely in this configuration. Another possibility is that this structure is located between us and the lensed system, along the line of sight. It could be a dust cloud and the perspective could make it seemingly encircling the four images. But again, we would be in special conditions. This structure remains thus quite mysterious. A very deep and highly resolved spectrum could allow the measurement of its redshift and would tell us where it is located comparing to the lensing galaxy. Such data are not available yet.

Unlike the case of H1413+117, the lensing galaxy is already obvious on the original frames of WFI J2033-4723. It is then worth trying to fit an analytical model on it. The latter being a part of the background, it will be constrained by the four frames of the set. After having tested both light profiles available with MCS, i.e. the de Vaucouleurs and exponential models, we conclude that a de Vaucouleurs profile is better adapted to model the main lensing galaxy of WFI J2033-4723. The results are summarized in Table 4.5. The columns show the following parameters: the PA[8] in degrees, the ellipticity, the effective semi-major and semi-minor axis. For each parameter, we list the standard deviation of the mean extracted from the individual deconvolutions of each frame. Let us insist on the fact that the listed value of the parameter itself is not the mean of the individual values, but the result coming from

---

[8]Let us recall that PA stands for *Position Angle* and is the angle that folds back the direction of the major axis over the direction of the North.

the simultaneous deconvolution. The PA is highlighted on the middle panel of Fig. 4.9.

Table 4.5: Lensing galaxy parameters for WFI J2033-4723 derived from the fit of a de Vaucouleurs profile. The first column presents the position angle in degrees. The usual sign convention is adopted: a positive angle corresponds to the anticlockwise direction. The ellipticity is given in the second column. The two last columns contain respectively the effective semi-major and semi-minor axis of the ellipse. Each measurement is accompanied by its 1σ error bars.

Position Angle (°)	Ellipticity	a_0 ($''$)	b_0 ($''$)
-152.2 ± 4.3	0.176 ± 0.026	0.665 ± 0.036	0.556 ± 0.025

4.2.4   Astrometry and photometry

The astrometric and photometric results extracted from the last iteration are listed in Table 4.6. They are derived the same way as we did for the Cloverleaf: we deconvolve each image individually except for the results concerning the galaxy which are better constrained on the simultaneous deconvolution. For each measure, the standard deviation of the mean obtained from the individual deconvolutions is provided. Of course, these are internal error bars. And as we have no image acquired in different conditionns, we cannot compare the results and thus cannot obtain reliable estimate of the external error bars.

We notice that the error bars of the magnitudes shown in the last column of Table 4.6 are larger by a factor two than those obtained for the Cloverleaf (see Table 4.1). There is no obvious explanation based on the deconvolution process itself: the results are quite satisfying when we look on the χ^2 and on the mean residual map.

One aspect of WFI J2033-4723 comes then to mind: the presence of this diffuse background surrounding the four lensed images. Let us compare it to the source C (see on the left panel of Fig. 4.9) which is the less-magnified image: their total flux are of the same order, the approximate magnitude of the halo in the Vega system being of 17.7. The latter value is estimated on the simultaneously deconvolved frame in subtracting the contribution of the galaxy itself from the total flux of the background (halo plus galaxy). Even if this method is quite coarse, it is enough for us to give the following conclusion: the halo can be partly responsible for the loss of accuracy in our photometry comparing to what we usually obtain with the iterative method.

Table 4.6: Relative astrometry and photometry for the four components of WFI J2033-4733 and its primary lens. The two coordinates are given in arcsecond relative to component B along the two usual directions: the right ascension and the declination. The photometry is given in apparent magnitude in the Vega system. For each measurement, we present the 1σ internal error bars.

ID	F160W		
	$\Delta\alpha$ ($''$)	$\Delta\delta$ ($''$)	Magnitude
B	0.	0.	17.767 ± 0.019
A1	-2.1946 ± 0.0004	1.2602 ± 0.0003	17.162 ± 0.021
A2	-1.4810 ± 0.0004	1.3756 ± 0.0005	17.518 ± 0.021
C	-2.1129 ± 0.0003	-0.2778 ± 0.0003	17.876 ± 0.020
G	-1.4536 ± 0.0020	0.3086 ± 0.0008	18.591 ± 0.026

Indeed, as the PSF is improved step by step in subtracting an approximate background, our process is very sensitive to any structure under the sources. The worst situation that can occur to us is an image with a flat and nearly constant background under each point source, which is exactly the case for WFI J2033-4723.

The previous reflection can lead to another one, related to the algorithm itself: the MCS version that we used when we treated WFI J2033-4723 did not allow to impose non-varying source intensities from one frame to the other[9]. In other words that means that the background in each frame is the same except for a multiplicative factor and an additive term but the intensities of the point sources are free to vary from one image to another (see Eq. 2.44): the ratio between the intensity of the sources and the background is not the same in each frame. And in certain cases, it seems to be more advantageous, in term of χ^2, to have a quite different ratio in the images. That will, of course, degrade the accuracy of the photometry. This nasty effect can be avoided with the new version of the algorithm in constraining the point sources and the background to have the same relative intensity in all images.

Let us compare our astrometric results with those obtained by Morgan et al. (2004) in treating the very same images. They are listed in Table 4.7. Our results are compatible with theirs within their error bars which are the dominating ones. The highest difference is observed for the position of the galaxy. This is not unexpected as a diffuse object is more sensitive to the

---

[9]The reason of this choice is simple: the algorithm was first used to obtain light curves of varying gravitationally-lensed systems.

image processing.

Table 4.7: Relative astrometry of WFI J2033-4723 obtained by Morgan et al. (2004). The two coordinates are given in arcsecond relative to component B along the two usual directions: the right ascension and the declination. The 1σ error bars are also given.

	F160W	
ID	$\Delta\alpha$ ($''$)	$\Delta\delta$ ($''$)
B	0.	0.
A1	-2.193 $\pm$ 0.03	1.258 $\pm$ 0.02
A2	-1.477 $\pm$ 0.03	1.368 $\pm$ 0.02
C	-2.108 $\pm$ 0.03	-0.282 $\pm$ 0.03
G	-1.412 $\pm$ 0.33	0.277 $\pm$ 0.20

4.3 WFI J2026-4536

4.3.1 Introduction

WFI J2026-4536 is another gravitationally-lensed system discovered in the same survey as WFI J2033-4723. It has the same kind of configuration but the maximum image separation amounts only to $1\rlap{.}''4$. The quasar is at a redshift of 2.23 and the total brightness of the system reaches 16.5 in the g filter. Apparently the environment is way less crowded than the one of WFI J2033-4723.

4.3.2 HST imaging

The four images of WFI J2026-4536 were obtained with NIC-2 through the F160W filter on the 21st of October 2003. They were taken in the MULTI-ACCUM mode: the first frame is a combination of 19 samples and has an exposure time of 639.9389 s while the three other frames are each a combination of 20 samples and have an exposure time of 703.9361 s. We use the images calibrated by CALNICA[10]. According to the version 6.3 of the Tiny Tim software (Krist & Hook, 2004), the mean pixel size of NIC-2 was of $0\rlap{.}''07568$ at the time of the observation. A combination of the four calibrated and reduced images of WFI J2026-4536 is shown on Fig. 4.10. Our reduction process is the same as for the Cloverleaf and is explained in section 4.1.2.

---

[10]Let us recall that CALNICA is the HST image reduction pipeline.
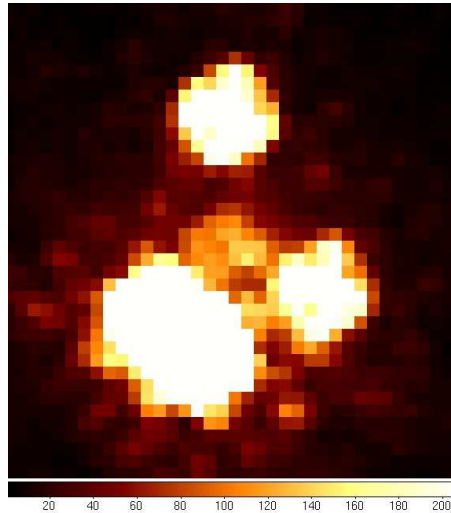
Figure 4.10: Combination of the four calibrated and reduced images of WFI J2026-4536 obtained with the F160W filter of NIC-2. The colour scale goes from 0% (black) to 2.1% (white) of the maximum intensity. North is to the top and East to the left.

4.3.3   Deconvolution

As no extra star is available in the field of WFI2026-4536, we use the iterative method to improve the Tiny Tim PSF and to separate possible diffuse structures from the point sources. We use the same sampling step and final PSF as for the two previous lensed systems: a sampling step 2 times smaller than the original pixel size and a Gaussian with a FWHM of 2 pixels for $\mathcal{R}(\vec{x})$, the final resolution of the images. These choices lead to an improvement of the resolution of the deconvolved frame comparing to the original images as well as a good sampling of the final light distribution.

After having reached the final iteration and analyzing the results, we noticed a problem in the astrometry and photometry: the individual results coming from the fourth image were different from the others and in taking them into account, the error bars were larger. We then suspected this image to be the node of the problem: there might be some pixels affected by cosmic rays or any other disease that we did not identify as such during the reduction phase. Unfortunately we could not find any of them. Still, we decided to remove the fourth image from our set of data. Indeed, this frame is much noisier than the other ones, which is not normal as all the observations were acquired in the very same conditions: there might have been an anomaly in the acquisition process.

The last step was thus redone with the first three images. In total,
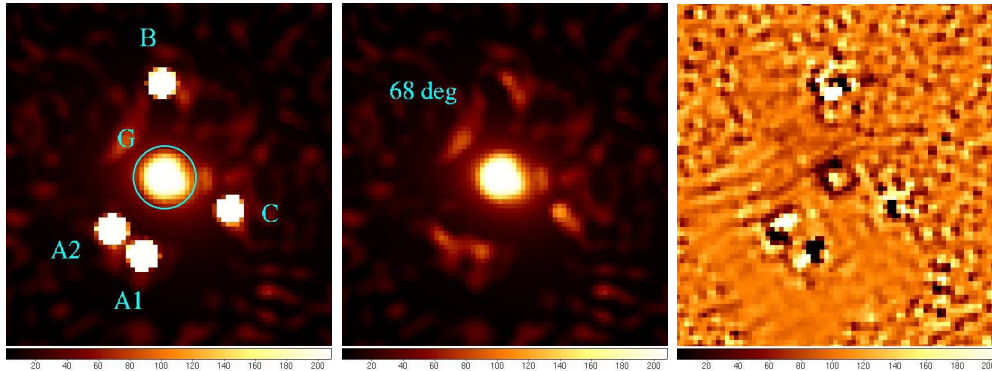
Figure 4.11: Results of the last simultaneous deconvolution for WFI J2026-4536. North is to the top and East to the left. *Left*: deconvolved frame, i.e. point sources plus smooth background; the point sources are labeled as in Morgan et al. (2004) and the lensing galaxy G is encircled. *Middle*: smooth background common to all images. *Right*: mean residual map of the simultaneous deconvolution.

four iterations were necessary to reach convergence and the final reduced χ^2 amounts to 4.73. The results are shown on Fig. 4.11. The mean residual map shown on the right panel indicates that there is no systematic structure under the point sources: the instrumental profile is well-adapted. The remnant structures are probably due to small variations of the PSF in the field of the CCD.

In this case, the primary lensing galaxy is already visible on the untreated images. As for WFI J2033-4723, it is thus very interesting to make use of an analytical model in the deconvolution algorithm to fit its light profile. This model, as a part of the diffuse background, will be constrained using the information available in the three frames. After having tested the exponential profile and the de Vaucouleurs profile, we conclude that the latter is better adapted to model this galaxy. The results of the best fit are shown in Table 4.8. The columns show the following parameters: the PA in degrees, the ellipticity, the effective semi-major and semi-minor axes. For each parameter, we calculate the standard deviation of the mean in deconvolving each frame individually. However the listed value of the parameter is not a mean value extracted from the individual deconvolutions, but the result of the simultaneous deconvolution. The PA is highlighted on the middle panel of Fig. 4.11.

Table 4.8: Lensing galaxy parameters for WFI J2026-4536 derived from the fit of a de Vaucouleurs profile. The first column presents the position angle given in degrees. The usual sign convention is adopted: a positive angle corresponds to the anticlockwise direction. The ellipticity is given in the second column. The two last columns contain respectively the effective semi-major and semi-minor axes of the ellipical galaxy. For each measurement, we present the 1σ error bars.

Position Angle ($°$)	Ellipticity	a_0 ($''$)	b_0 ($''$)
68.5 ± 7.9	0.243 ± 0.042	0.583 ± 0.073	0.747 ± 0.050

4.3.4 Astrometry and photometry

The astrometric and photometric results of the last deconvolution are exposed in Table 4.9 as well as the error bars. They are the standard deviations of the mean and they were derived the same way as for the Cloverleaf and WFI J2033-4723: in deconvolving individually each frame of the set. Here again, they are internal: we have no image acquired with another instrument configuration and thus we cannot compare the results to obtain an estimation of the external error bars.

Let us compare our astrometric results with those listed in Table 4.10 (Morgan et al., 2004). They were also obtained with the NIC-2 F160W set of images. Our position of the lensed images are very close to theirs and are compatible within their error bars. As usual, the accuracy on the galaxy position is not as good as the one on the position of the point sources. They are not compatible within the 1σ error bars for the right ascension but they are in agreement for the declination. A fainter and diffuse component is always more sensitive to the image processing and to any inaccuracy in the recovered PSF.

Table 4.9: Relative astrometry and photometry for the four components of WFI J2026-4536 and its lens galaxy. The two coordinates are given in arc-second relative to component B along the two usual directions: the right ascension and the declination. The photometry is given in apparent magnitude in the Vega system. For each measurement, we present the 1σ error bars.

ID	F160W		
	$\Delta\alpha$ ($''$)	$\Delta\delta$ ($''$)	Magnitude
B	0.	0.	17.054 ± 0.007
A1	0.1622 ± 0.0003	-1.4279 ± 0.0003	15.586 ± 0.002
A2	0.4150 ± 0.0003	-1.2135 ± 0.0002	16.019 ± 0.006
C	-0.5717 ± 0.0003	-1.0440 ± 0.0001	17.272 ± 0.005
G	-0.0475 ± 0.0013	-0.7912 ± 0.0017	19.456 ± 0.046

Table 4.10: Relative astrometry of WFI J2026-4536 obtained by Morgan et al. (2004). The two coordinates are given in arcsecond relative to component B along the two usual directions: the right ascension and the declination. The 1σ error bars are given.

ID	F160W	
	$\Delta\alpha$ ($''$)	$\Delta\delta$ ($''$)
B	0.	0.
A1	0.1621 ± 0014	-1.4281 ± 0.0009
A2	0.4149 ± 0014	-1.2133 ± 0.0009
C	-0.5722 ± 0015	-1.0436 ± 0.0004
G	-0.0813 ± 0031	-0.7967 ± 0.0068

Chapter 5

Conclusions

We have elaborated a new image processing method, based on the MCS deconvolution algorithm, which allows, at the same time, the determination of the PSF of images and their deconvolution. This procedure is applicable to images which contain at least two point sources so that the algorithm can separate the contributions of background objects from those of the instrumental profile itself.

This technique is particularly well-suited to the analysis of multiply-imaged quasars: it allows the detection of extended structures such as lensing galaxies, arcs or rings. It provides accurate astrometry and photometry of the multiple images and of the lens, which is very important for modeling the system. This technique has been applied on HST NIC-2 images of three gravitationally-lensed quasars: H1413+117 (the Cloverleaf), WFI2033-4723 and WFI2026-4536.

Let us summarize our results on the Cloverleaf. The internal error on the source positions, taking into account the error coming from the deconvolution only, is of the order of 0.4 milliarcsec. When comparing the astrometry coming from two different sets of images, we find an external error of the order of 1 milliarcsec. It probably finds its origin in an incomplete correction of the geometric distortions. Moreover, we detect the lensing galaxy and measure its position with an accuracy of ~ 20 milliarcsec. We also discover a partial Einstein ring, which should allow us to constrain the deflection model and, through an inversion of the lens equation, to estimate the light

distribution in the quasar host galaxy and narrow line region.

In the second lensed quasar that we investigate, i.e. WFI2033-4723, the maximum internal error on the position of the point sources amounts to 0.5 milliarcsec. We also detect the main lensing galaxy and fit a de Vaucouleurs profile on its surface brightness: that brings further constraints as the PA or the ellipticity to be used when modeling the whole lensed system. We also detect a faint and relatively flat diffuse background encircling the four images and the lens. That structure remains quite mysterious for the moment: further investigations are necessary.

In our last case, WFI2026-4536, the internal error on the position of the lensed images amounts to 0.3 milliarcsec at most. The main lensing galaxy, already detected before image processing, is highlighted after a simultaneous deconvolution of three images of the set, the fourth one being damaged. We also fit a de Vaucouleurs profile on this lens, which, as already mentioned, is very important to constrain the lens model.

For the three first gravitationally-lensed systems under investigation, the application of our iterative method using the MCS algorithm is a success. Since they were treated, some modifications have been made to the algorithms and to the reduction process. They were tested on several objects, mostly gravitationally-lensed quasars, and have lead to improvements on certain points of the procedure. However, no matter the version of the algorithm used, it often demands carefulness and perseverance to obtain such results. But it always requires a sharp intuition on the object which nature we want to unveil.

Chapter 6

About the next step towards H_0: modeling strong lensing

One of the most important applications of gravitational lensing is, as already mentioned, the determination of the Hubble constant, H_0. To be able to do so, we need to have:

1. a measurement of the time delay between at least two lensed images of the system. This non trivial task can be carried out on light curves obtained by monitoring the object on a long-term period and with high photometric accuracy;

2. a pretty accurate estimation of the lens mass distribution, which can be obtained with results coming from an adequate treatment of high resolution images.

Of course, this latter point is now within our reach as we developed an image processing technique able to provide accurate astrometry and photometry of images containing a non-negligible background plus point sources.

The first point is carried out by other members of the COSMOGRAIL collaboration. Let us recall that COSMOGRAIL stands for COSmological MOnitoring of GRAvItational Lenses. This collaboration, which started in April 2004, brings astrophysicists from different countries together: Switzerland, Belgium, England and Uzbekistan. The COSMOGRAIL program is the following: monitoring lensed quasars (for the moment approximately 30) to obtain well-sampled light curves. The aim is to measure accurate time

delays in order to derive H_0. The data are obtained with four small telescopes located in the northern and southern hemispheres: the Swiss Euler telescope at La Silla in Chile, the Belgian-Swiss Mercator telescope in La Palma (Canary Islands, Spain), the telescope of Maidanak Observatory in Uzbekistan and the Himalayan Chandra telescope in India. For the moment, the COSMOGRAIL members are mainly working on WFI J2033-4723, e.g. Christel Vuissoz from the Swiss node is responsible for the calculation of the time delay and Dominique Sluse, also from the Swiss node, is in charge of the modeling part and is thus using our results.

But what else do we need to model a gravitationally-lensed system? Indeed, positional constraints from high resolution images are not enough: some other observational parameters are necessary. The distance to the source and the distance to the lens are very important. Even if most of the lensing galaxies are not faint, their redshift is far from being trivial to derive. But a technique based on the MCS algorithm allows the spatial deconvolution of spectra: it has proved to be very useful and has permitted to obtain some lens redshifts from ground-based data. In other cases (e.g. a larger image separation or a brighter lens), the lens spectra can be obtained by traditional techniques such as simple slit spectroscopy.

Another difficulty can be pointed out: an isolated lens bending the light from a background quasar is fairly rare. Indeed, galaxies are distributed in groups or clusters. So, most of the time, when a lensed system is observed, there are other objects relatively close to the line of sight that perturb the potential and thus modify the image positions, the time delays and the inferred value of H_0. This phenomenon is taken into account through a shear in the galaxy model. Unfortunately that causes a degeneracy: the observed configuration of images can be reproduced by several mass models.

Two options are to consider when modeling strong lenses: whether to do it with a parametric model as it is the case in the *gravlens* algorithm of Keeton (2001b) and Keeton (2004), or with a free form lens model as in the *pixelens* algorithm of Saha & Williams (1997) and Williams & Saha (1999). The first solution relies on analytical models such as the singular isothermal sphere (SIS). In this model, the mass components behave like particles in an ideal isothermal gas and the deflection angle does not depend on the impact parameter (Keeton, 2001a). In the second option the mass distribution is not restricted to any shape: the model is created from lots of small independent mass elements called *pixels*. Let us mention that quadruply-imaged quasars bring more constraints than doubly-imaged quasars, which is not to be neglected for the construction of a model.

Until now the determination of mass distributions has lead to large uncertainties, which is problematic for the calculation of H_0. But the problem

can be taken the other way: if H_0 is measured by a completely independent technique, the time delay can bring non-negligible extra constraints to the model and in particular, to the composition and structure of dark matter halos (Schechter & Wambsganss, 2002).

This topic is worth further investigations: this is the subject of another work that will be carried out by Eva Eulaers who is also a member of the COSMOGRAIL collaboration.

Appendix A

Related paper

The paper related to the Cloverleaf and to the presentation of the new iterative method based on the MCS algorithm is shown on the following pages. It was accepted on the 28th of March 2007 and will be published soon in *Astronomy & Astrophysics*.

Deconvolution of HST images of the Cloverleaf gravitational lens

Detection of the lensing galaxy and a partial Einstein ring

V. Chantry and P. Magain

Deconvolution of HST images of the Cloverleaf gravitational lens ⋆

Detection of the lensing galaxy and a partial Einstein ring

V. Chantry ⋆⋆ and P. Magain

Institut d'Astrophysique et de Géophysique, Université de Liège, Allée du 6 Août, 17, Sart Tilman (Bat. B5C), Liège 1, Belgium

ABSTRACT

Archival HST/NICMOS–2 images of the *Cloverleaf* gravitational lens (H1413+117), a quadruply–imaged quasar, were analysed with a new method derived from the MCS deconvolution algorithm (Magain et al., 1998). This method is based on an iterative process which simultaneously allows us to determine the Point Spread Function (PSF) and to perform a deconvolution of images containing several point sources plus extended structures. As such, it is well–adapted to the processing of gravitational lens images, especially in the case of multiply–imaged quasars. Two sets of data were analysed: the first one, which was obtained through the F160W filter in 1997, basically corresponds to a continuum image, while the second one, obtained through the narrower F180M filter in 2003, is centered around the forbidden [OIII] emission lines at the source redshift, thus probing the narrow–line region of the quasar. The deconvolution gives astrometric and photometric measurements in both filters and reveals the primary lensing galaxy as well as a partial Einstein ring. The high accuracy of the results is particularly important in order to model the lensing system and to reconstruct the source undergoing the strong lensing. The reliability of the method is checked on a synthetic image similar to H1413+117.

Key words. Gravitational lensing: Einstein ring, lensing galaxy – Techniques: image processing, MCS deconvolution algorithm – Quasars: Cloverleaf, H1413+117

1. Introduction

Four years after its discovery by Hazard et al. (1984), the quasi–stellar object (QSO) H1413+117 was identified as a gravitational lens by Magain et al. (1988). This system, consisting in 4 components of comparable brightness separated by ~ 1 arcsec, is best known as the *Cloverleaf*. It is also one of the brightest quasars amongst the BAL (Broad Absorption Line) class, with a redshift of 2.558 and an apparent visual magnitude of 17. The lensing galaxy was detected by Kneib et al. (1998) from a careful PSF subtraction on near–infrared Hubble Space Telescope (HST) images.

The aim of the present paper is to present a method which simultaneously allows us to perform PSF determination and deconvolution on images containing several point sources superimposed on a diffuse background, and to apply it to HST images of the Cloverleaf gravitational lens. We show that this method permits a more accurate astrometry of the system and a better characterisation of the lensing galaxy. Moreover, it also allows the detection of additional structures, such as parts of an Einstein ring.

This method is based on the MCS deconvolution algorithm (Magain, Courbin & Sohy, 1998) which, unlike most deconvolution methods, ensures that the deconvolved image, which has a well–defined Point Spread Function (PSF), conforms to the sampling theorem. The method also leads to a decomposition of the light distribution into a sum of point sources (of known shape) and a diffuse background.

More recently, Magain et al. (2006) presented a method, derived from MCS, to determine the PSF on images consisting of (possibly blended) point sources. This method works well, even in very crowded fields, when no point source is sufficiently isolated to derive an accurate PSF from standard techniques.

The algorithm presented here extends the method of Magain et al. (2006) to images containing a mixture of point sources and diffuse background. It is based on an iterative scheme, in which both the PSF and the diffuse background are improved step–by–step.

In section 2 we describe the input data and their reduction. The method used to obtain both the PSF and the deconvolved images is described in section 3. The results are presented and discussed in section 4. The accuracy of our results is tested by applying the method to a synthetic image with the same basic configuration as the Cloverleaf (see section 5). Finally, we conclude in section 6.

---

2   V. Chantry and P. Magain: Deconvolution of HST images of the Cloverleaf gravitational lens

2. HST Images

The first set of HST data was obtained on the 28th of December 1997 by the camera 2 of NICMOS (Near Infrared Camera and Multi–Object Spectrometer) with the F160W filter (wide band filter), corresponding approximately to the near–IR H–Band (PI: E. Falco). We used the 4 calibrated images, i.e. treated by the HST image reduction pipeline (CALNICA). Each of them has an exposure time of 639.9389 s and a mean pixel size of $0\rlap{.}''07510$ according to Tiny Tim[1] software v 6.3 (Kris & Hook, 2004). These images were obtained in the MULTIACCUM mode: each of them is a combination of several samples (19 in the present case). A combination of these 4 images is shown on the left panel of Fig. 1.
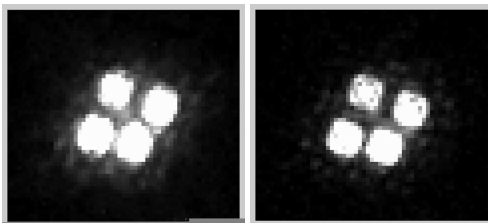

Fig. 1. *Left*: combination of the 4 calibrated images from the F160W filter data set obtained with the HST/NICMOS–2, the grey scale going from 0% (black) to 3.2% (white) of the maximum intensity; *Right*: combination of the 8 calibrated images from the F180M filter data set obtained with the HST/NICMOS–2, the grey scale going from 0% (black) to 4.7% (white) of the maximum intensity. The structure of the PSF is obvious. North is to the top and East to the left.

The second set of images was obtained on the 10th of July 2003 with the same instrument and the F180M medium–band filter (PI: D. A. Turnshek). As for the F160W filter we used the calibrated images, here 8 images, 4 of them being a combination of 18 samples and the other 4 being a combination of 16 samples. The first 4 have an exposure time of 575.9418 s and the latter 4 an exposure time of 447.9474 s. The mean pixel size is, again according to Tiny Tim software, $0\rlap{.}''07568$. A combination of these calibrated images is shown on the right panel of Fig. 1.

The wavelength ranges of these two filters are partly superimposed: the passband of the F160W filter is $1.4 \, \mu m \leq \lambda \leq 1.8 \, \mu m$ while it amounts to $1.76 \, \mu m \leq \lambda \leq 1.83 \, \mu m$ for the F180M filter. The latter was chosen in order to include the oxygen [OIII] forbidden–line doublet $(499 - 501 \text{ nm})$ at the redshift of the QSO.

The image reduction is divided into two parts: the image cleaning and the calculation of the sigma images (i.e. images containing the standard deviations of the pixel intensities). The first step of the first part consists in computing the intensities in counts per pixel. The second step consists in removing the sky background. As the NIC–2 detector is composed of 4 quadrants, it is necessary to subtract a different constant value for each of them. These constants

were derived from the parts of the image where there is no obvious light source.

The second step consists in the calculation of the sigma images. We start from the sigmas calculated by the pipeline CALNICA. Two effects are then corrected. First, we take into account the underevaluation of the standard deviation for the negative pixels (by replacing all negative intensities by a null value). Secondly, we make use of the HST flag files indicating bad pixels, e.g. cold or hot pixels. It allows us, using the inverted sigma images, to put the statistical weight of such bad pixels to zero so that the information they provide has no weight in the deconvolution.

Let us mention that we do not remove the cosmic–ray impact from the images during the reduction process. We use the deconvolution residuals (see below) to spot the pixels likely of having been contaminated by a cosmic ray. We then put the inverted sigma value of such pixels to zero.

All these manipulations are carried out with the IRAF[2] package.

3. Method

The same technique, based on the MCS deconvolution algorithm, was applied to both sets of images in order to improve their resolution and sampling and, most importantly, to detect any significant extended structure which might be hidden by the complex PSFs. The method is based on the simultaneous deconvolution of all images from a set, as explained, e.g., in Courbin et al. (1998). This means that we attempt to find a light distribution that is compatible with all images obtained in a given instrument configuration (e.g. through a given filter). To do this we allow a spatial translation in between the individual images and, in some cases, a variation of the point source intensities. In order to improve the resolution while keeping a well–sampled light distribution, we use a sampling step 2 times smaller than the original pixel size and we choose, as the final PSF (i.e. the PSF of the deconvolved images), a Gaussian with 2 pixels Full–Width–at–Half–Maximum (FWHM). Let us mention that, since the HST PSF varies with the position in the focal plane, and since the object is located in different parts of the detector at each exposure, each original image has its own individual PSF.

The originality of the present method is that the same images are used both to determine the PSF and to perform the deconvolution (basically to detect the diffuse background and to obtain the astrometry and photometry of all objects). It works only if there are several point sources in the field: this makes it possible to distinguish the structure belonging to the PSF (and thus appearing in the vicinity of each point source) from the diffuse background, assumed not to be identical around each source.

This new method is based on an iterative process. We start with a first approximation of the PSF constructed by the Tiny Tim software (see Fig. 2) with a sampling step two times smaller than the original one. That PSF is deconvolved by the final Gaussian PSF in order to obtain the deconvolution kernel that we call the PSF $s_0(x)$. This

---

[1] Tiny Tim is a software package which allows the generation of the HST Point Spread Function for each instrument, filter and observing configuration.

[2] IRAF, Image Reduction and Analysis Facility, is distributed by the National Optical Astronomy Observatories, which are operated by AURA, the Association of Universities for Research in Astronomy, Inc., under cooperative agreement with the NSF, National Science Foundation.

is a reasonable first approximation, although not accurate enough to obtain trustworthy deconvolved images. Indeed, when using that PSF for deconvolving the original images, which we call $d_0(\boldsymbol{x})$, significant structure appears around each point source, clearly showing that the Tiny Tim PSF departs from the actual one (see Fig. 3).

Since no extra images of stars are available in the field to improve this PSF, we have to use the information in the point sources of the Cloverleaf itself. However, we know that there might be some extra structure under the 4 point sources, as well as a contribution from the lensing object. That is why we proceed as follows:

1. First, for each individual image, we determine an improved PSF following the method described in Magain et al. (2006). This is done by adding a numerical background to the approximate PSF, $s_0(\boldsymbol{x})$) (here, the deconvolved Tiny Tim PSF), so that the observed image $d_0(\boldsymbol{x})$ is reproduced better. But, since this method assumes the image contains only point sources, and since our object contains a diffuse component, a part of it will be wrongly included in the improved PSF $s_1(\boldsymbol{x})$. If the structure of the diffuse component were identical around each point source, it would be entirely included in the PSF. On the other hand, if it were completely different around each of the four point sources, only $\sim 25\%$ of it would be included in the PSF. In practice, a variable fraction of that diffuse component goes into the PSF. As long as that fraction is below 100%, our iterative procedure will allow improvement of the results.
2. We then use that improved PSF $s_1(\boldsymbol{x})$ to perform a simultaneous deconvolution of all images ($s_1(\boldsymbol{x})$ varies slightly from image to image). This allows us to obtain a first approximation of the diffuse background $b_1(\boldsymbol{x})$. By construction, $b_1(\boldsymbol{x})$ is the same in all images. However, since a part of the actual background was included in the PSF $s_1(\boldsymbol{x})$, $b_1(\boldsymbol{x})$ is the only remaining part of the actual background.
3. We subtract $b_1(\boldsymbol{x})$, reconvolved and resampled to the initial resolution, from the original images. This gives us a new version of the observed images, $d_1(\boldsymbol{x})$, containing a lower amount of diffuse background. The first iteration is over.
4. To begin the second iteration, we use these images $d_1(\boldsymbol{x})$ to determine improved PSFs $s_2(\boldsymbol{x})$. As $d_1(\boldsymbol{x})$ contains a
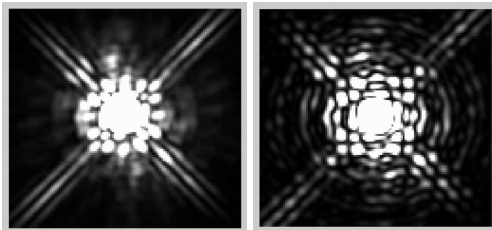

Fig. 2. PSF constructed by the Tiny Tim software for one of the frames in each set. We can easily see the spikes and the complex structure of the NIC–2 PSFs whatever the filter. *Left*: F160W, the grey scale goes from 0% (black) to 0.13% (white) of the peak intensity; *Right*: F180M, the grey scale goes from 0% (black) to 0.16% (white) of the peak intensity.
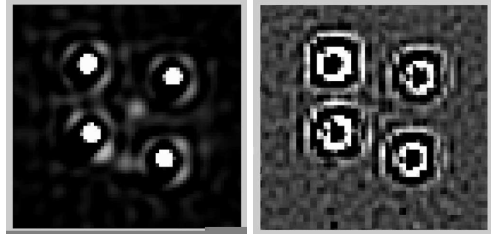

Fig. 3. Results of the simultaneous deconvolution for the F160W data set using a deconvolved Tiny Tim PSF. *Left*: deconvolved image, the grey scale going from 0% (black) to 0.45% (white) of the maximum intensity. *Right*: residuals (see text) of the deconvolution. The remnant structure around each point sources is obvious.

lower amount of background than $d_0(\boldsymbol{x})$, the new PSFs are indeed closer to the correct ones.
5. The simultaneous deconvolution of the original images $d_0(\boldsymbol{x})$ with the new PSFs $s_2(\boldsymbol{x})$ allows us to get a diffuse background $b_2(\boldsymbol{x})$ which is improved with respect to the one obtained at the previous iteration.
6. We subtract $b_2(\boldsymbol{x})$ from the original images $d_0(\boldsymbol{x})$. This closes the second iteration.
7. The iterative procedure is continued until no significant improvement is observed. Usually around 4–5 iterations are necessary, depending on the structure under the sources.

4. Results

4.1. Iterative Process

We now consider the application of this iterative process to the two sets of HST/NIC–2 images of the Cloverleaf.

For the F160W data set, 7 iterations were necessary while, for the F180M data set, convergence was reached after 3 iterations. This difference is due to the fact that the diffuse background is less intense relative to the point sources in the latter filter. Figures 4 and 5 illustrate the evolution of the PSF in the iterative scheme: they show the corrections applied at different stages. We can see that the first step of the iterative process changes significantly the PSF obtained with Tiny Tim. The next steps allow smaller adjustments and smaller details. In the case of the F180M filter, it is obvious that only 3 iterations are necessary, as the corrections already become negligible after the second step. The same happens after the sixth iteration for the F160W data set.

Now that we have an idea about the evolution of the PSFs, we can focus on the results of the deconvolution itself. Figures 6 and 7 show the deconvolved frames from the last iteration, respectively for the F160W and the F180M data set. The partial Einstein ring, which is the gravitationally lensed image of the quasar host galaxy, and the lensing object can be seen for both sets on the background frame (top left) and on the background plus point source frame (top right). The lens galaxy appears less intense compared to the point sources in the F180M filter, which is expected as this is a medium–band filter including the [OIII] emission lines (499–501 nm) at the redshift of the QSO and no

4   V. Chantry and P. Magain: Deconvolution of HST images of the Cloverleaf gravitational lens

expected emission line at the redshift of the lens. The partial Einstein ring also has a different structure: compared to the F160W filter, it appears more intense close to the point sources and less intense in between them. This suggests that the narrow–line region (NLR) is more compact than the global lens galaxy, which could have been expected.

The residuals r_i from the deconvolution after the ith iteration are defined as follows:

$$r_i(\boldsymbol{x}) = \frac{m_i(\boldsymbol{x}) - d_0(\boldsymbol{x})}{\sigma_0(\boldsymbol{x})} \qquad (1)$$

where m_i stands for the reconvolved model after the ith iteration, $d_0(\boldsymbol{x})$ for the observed image and $\sigma_0(\boldsymbol{x})$ for the standard deviation of this image. The residual map, as shown on the bottom left of Figs. 6 and 7, is an important source of information: it guides us through the different steps. We can see there is some structure left under the point sources, but nothing systematic, and there is nearly no remnant structure where the ring and the lensing galaxy are located. The fact that the residuals under the four point sources have very different shapes suggests that they are not due to PSF errors, but rather to small PSF variations from one QSO image to another.

Another important guide through the different stages of the process is the reduced chi squared (χ_r^2) which, theoretically, should be close to unity for a perfect deconvolution with a perfect PSF. In the last iterations it barely changes: the PSF is not improved significantly anymore and the iterative process has converged. We calculate it for each set and each iteration step in the zone of interest, i.e. in a square containing the four point sources and the extended structures (ring plus lens). We obtain a χ_r^2 of 3.845 after the seventh iteration for the F160W data set, and a χ_r^2 of 1.125

Fig. 5. Corrections applied to the PSFs at different stages of the process for one of the images of the F180M data set. The grey scale goes from -4.8% (black) to +4.8% (white) of the peak intensity of the deconvolved Tiny Tim PSF. *Left*: corrections to the PSF in the first iteration (starting from the deconvolved Tiny Tim PSF). *Right*: corrections at the last iteration

Fig. 6. Final results of the simultaneous deconvolution for the F160W data set. North is to the top and East to the left. *Top left*: smooth background common to all images of the set where the lensing galaxy is encircled. *Top right*: deconvolved image (point sources plus smooth background); the point sources are labelled as in Magain et al. (1988). *Bottom left*: mean residual map of the simultaneous deconvolution. *Bottom right*: image reconvolved to the instrument resolution, with the point sources removed.
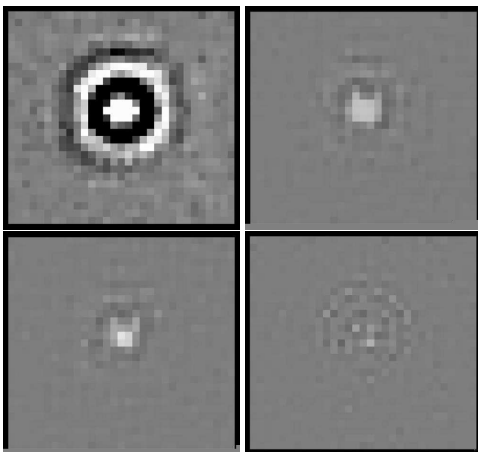

Fig. 4. Corrections applied to the PSFs at different stages of the process for one of the images of the F160W data set. The grey scale goes from -2.6% (black) to +2.6% (white) of the peak intensity of the deconvolved Tiny Tim PSF. *Top left*: corrections to the PSF in the first iteration (starting from the deconvolved Tiny Tim PSF). *Top right*: corrections at the second iteration. *Bottom left*: corrections at the fourth iteration. *Bottom right*: corrections at the last iteration.
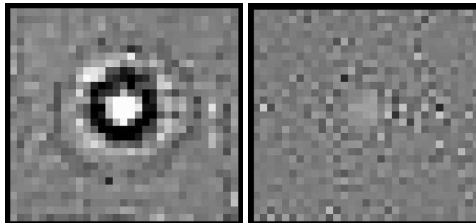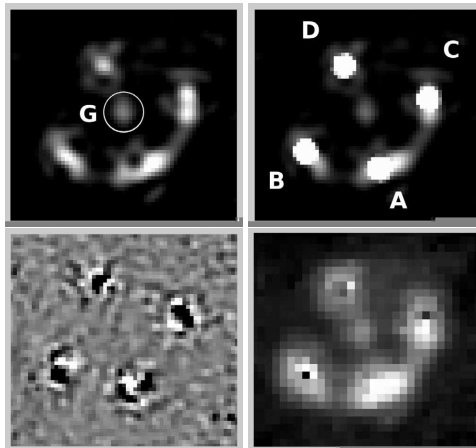
for the F180M data set after the third iteration, which is really good. Let us mention that these values are computed taking into account all images of a given set, so that any slight incompatibility between some of the input images results in an increase of the χ^2 that cannot be lowered by changing the model. A final χ_r^2 of 1 means that the model is perfectly compatible with all the images of the set. It implies that all the images are statistically compatible with each other and that the PSF is perfectly known. Any inaccuracy in the data acquisition or reduction will increase the final χ^2.

4.2. Astrometry and photometry

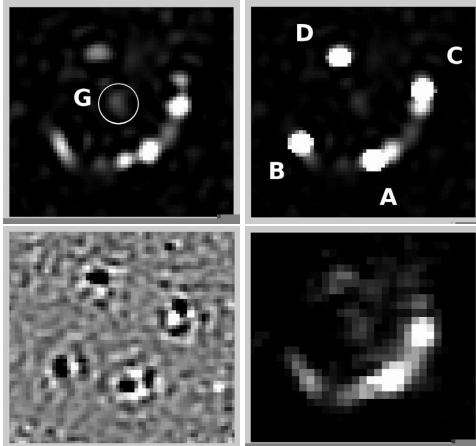Table 1 gives the relative astrometry and photometry for the quasar images as well as for the lens galaxy in both

V. Chantry and P. Magain: Deconvolution of HST images of the Cloverleaf gravitational lens   5

Fig. 7. Final results of the simultaneous deconvolution for the F180M data set. North is to the top and East to the left. *Top left*: smooth background common to all images of the set where the lensing galaxy is encircled. *Top right*: deconvolved image (point sources plus smooth background); the point sources are labelled as in Magain et al. (1988). *Bottom left*: mean residual map of the simultaneous deconvolution. *Bottom right*: image reconvolved to the instrument resolution, with the point sources removed.

filters. The coordinates are measured relative to component A (see Figs. 6 and 7). The apparent magnitudes are given in the Vega system.

As the geometric distortions depend on the position on the detector, their proper corrections require an individual deconvolution of each image. We then obtain the position of each point source (relative to source A) on each deconvolved image, corrected for distortion according to the formulae given in the NICMOS Data Handbook (Noll et al., 2004), and compute average values. For the point sources, this gives more accurate results than a simultaneous deconvolution with a mean correction on the coordinates. On the other hand, this is not true for the lensing galaxy and Einstein ring. As these are much fainter objects, it is better to rely on the results of the simultaneous deconvolution, where the signal in the whole set of images is used to constrain the shape of these objects. A mean geometric correction can then be applied, whose internal errors are lower than the random uncertainties on these fainter components.

The error bars given in Table 1 are internal errors. They are calculated by deconvolving each image individually and comparing the coordinates and magnitudes obtained. The listed values are the standard deviation of the means.

The astrometric precision for the point sources is about 0.5 milliarcsec in the F160W filter and 0.3 milliarcsec in the F180M filter. The higher precision in the medium band filter may be explained by the fact that the partial ring and the lens galaxy appear fainter relative to the point sources and thus have a lower contribution to the error bars.

Of course, the precision on the position of the lens galaxy is significantly lower. This is due to the facts that (1) it is a diffuse object; (2) it is much fainter than the point sources (about 4.5 mag in the F160W filter and 6.4

mag in the F180M filter) and (3) it is mixed with the PSF wings of the point sources.

Table 1 also shows that the results derived from both filters are not compatible within their internal error bars. As the geometry of the system is not expected to vary on the time scale of a few years, this disagreement suggests that the actual error bars are significantly larger than the internal errors. The causes may be diverse. As the two sets of data were acquired 6 years apart, with a different orientation of the HST and thus of the detector, and in different cycles of NICMOS (pre– and post–NCS, NICMOS Cooling System), some geometrical distortions may not have been completely taken into account. The uncertainties concerning the coefficients of the formulae used to correct for the geometrical distortions, as given in the NICMOS Data Handbook (Noll et al. 2004), account for an uncertainty of the order of 0.1 milliarcsec in each filter, which is about an order of magnitude smaller than the external errors we obtain. It is thus possible that a residual distortion of the NICMOS images remains, at the 10^{-3} level (0.001 arcsec per arcsec). An imperfect separation of the partial Einstein ring from the point sources in the deconvolution process as well as some inaccuracies in the PSF recovery may also play a role.

The external errors, computed by comparing the source positions derived from the two data sets, are the following: the average difference between the point source positions amounts to 1.4 milliarcsec. Assuming that the errors in both data sets contribute equally to this difference, we derive a value of $1.4/\sqrt{2} \approx 1$ milliarcsec (i.e. 0.013 pixel) for the estimated accuracy in the position of the point sources.

Our measurements are compared to those of Magain et al. (1988) and Turnshek et al. (1997) in Table 2. The latter were derived from images acquired with another HST intrument (Wide Field Planetary Camera) and with a completely different image processing technique, while the first ones were obtained from much lower resolution ground-based images. For both sets of results we indicate the 1 σ error bars (which do not appear in the original paper of Magain et al.). The average difference between our results and those of Magain et al. (1988) amount to 4 milliarcsec, which approximates the error bars on the measurements performed by these authors. The same comparison with Turnshek et al. (1997) gives an average difference of 2.6 milliarcsec, also compatible with their error bars.

The primary lens, a single galaxy, was detected in 1998 by Kneib et al. After a PSF subtraction of the four lensed images they obtained the following relative positions for the lensing galaxy:

$$\alpha = 0.112'' \pm 0.02''$$

and

$$\delta = 0.503'' \pm 0.02''$$

Their lens position is compatible with our result in right ascension ($\Delta\alpha = -0.025 \pm 0.020$). But this is not true for the declination ($\Delta\delta = -0.086 \pm 0.020$). Possible systematic errors, in particular on the lens position, are investigated in the next section.

Finally, as already mentioned, the intensity distribution along the partial Einstein ring is significantly different in the two filters: it is more regular in the wide band F160W

6   V. Chantry and P. Magain: Deconvolution of HST images of the Cloverleaf gravitational lens

Table 1. Relative astrometric and photometric measurements for the four components of the system and the lensing galaxy (G). The right ascensions α and the declinations δ are given in arcsecond relative to component A. The photometry is given in apparent magnitudes in the Vega system. The internal 1 σ error bars are also indicated (see text for an explanation on how they are derived).

ID	F160W			F180M		
	$\Delta\alpha$ ('')	$\Delta\delta$ ('')	Magnitude	$\Delta\alpha$ ('')	$\Delta\delta$ ('')	Magnitude
A	0.	0.	15.760 ± 0.002	0.	0.	15.548 ± 0.006
B	0.7426 ± 0.0002	0.1686 ± 0.0004	15.863 ± 0.005	0.7458 ± 0.0003	0.1688 ± 0.0002	15.650 ± 0.009
C	-0.4930 ± 0.0003	0.7135 ± 0.0004	16.143 ± 0.004	-0.4917 ± 0.0003	0.7105 ± 0.0003	15.902 ± 0.004
D	0.3526 ± 0.0007	1.0394 ± 0.0004	16.400 ± 0.006	0.3532 ± 0.0003	1.0400 ± 0.0002	16.218 ± 0.007
G	0.1365 ± 0.0024	0.5887 ± 0.0035	20.527 ± 0.037	0.1255 ± 0.0036	0.6192 ± 0.0069	22.182 ± 0.101

Table 2. Relative astrometry of the Cloverleaf from Magain et al. (1988) and from Turnshek et al. (1997). The right ascension α and the declination δ are given in arcsecond relative to component A. The 1 σ error bars are also indicated.

ID	Magain et al. (1988)		Turnshek et al. (1997)	
	$\Delta\alpha$ ('')	$\Delta\delta$ ('')	$\Delta\alpha$ ('')	$\Delta\delta$ ('')
A	0.	0.	0.	0.
B	0.753 ± 0.006	0.173 ± 0.006	0.744 ± 0.003	0.172 ± 0.003
C	-0.496 ± 0.004	0.713 ± 0.003	-0.491 ± 0.003	0.716 ± 0.004
D	0.354 ± 0.004	1.043 ± 0.004	0.355 ± 0.003	1.043 ± 0.012

filter than in the narrower F180M one. As the latter filter was chosen to emphasize the [OIII] emission lines (499–501 nm) and thus to obtain a mapping of the narrow emission line region in the quasar host galaxy, such a difference is not unexpected. The partial ring observed in the broad–band filter is a distorted image of the full host galaxy, while the narrow emission–line region is more prominent in the F180M filter. In particular, two bright knots are seen close to the A and C images of the quasar in Fig. 7. These knots cannot correspond to deconvolution artifacts, which might be caused, e.g., by an imperfect modelling of the PSF. Indeed, such artifacts would be expected around all point sources and at the same position relative to these point sources, which is not the case. Moreover the observed positions fit well with the inverted parity expected between two neighbouring images in such a lensed system. These bright knots must therefore correspond to the emission line region in the quasar host galaxy, which is thus probably brighter on one side than on the other. A detailed modelling of the system, including an inversion of the lens equation, should allow the reconstruction of an image of the host galaxy and of the narrow line region. This would be the first time one could map the host and narrow line region of a BAL QSO at such a high redshift.

5. Synthetic Image

The accuracy of our results is further tested by carrying the same procedure on a synthetic image having characteristics similar to those of the HST/NICMOS F160W Cloverleaf image: 4 point sources, a faint lensing object and a partial Einstein ring (see Fig. 8). This synthetic image was convolved with a PSF similar to the actual one, but unknown to the test performer. Random noise was then added to get a S/N comparable to that of the combined HST image (see Fig. 9).

The results obtained after three iterations are presented on Fig. 10, which displays the background alone, the point sources plus background, and finally the residual map. Some remnant structures can be seen under the point sources on the residual map. They are slightly weaker than
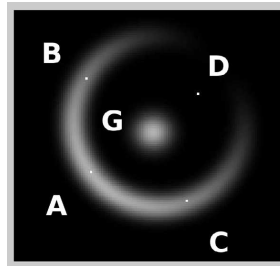

Fig. 8. Synthetic image of a gravitationally–lensed quasar with a configuration similar to the Cloverleaf: 4 point sources, a faint lensing object, and a partial Einstein ring. The orientation is the same as the original F160W Cloverleaf images.
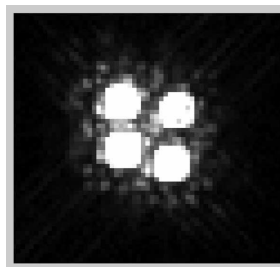

Fig. 9. Synthetic image convolved with a HST-type PSF unknown to the test performer and with added random noise similar to the actual observation.

those observed in the residual maps of the actual images, but show similar characteristics.

On average, the flux in the background (ring + lens) is recovered within 4%, which can be considered as excellent since this diffuse background is very weak compared to the point sources. However, because of the smoothing constraint, the deconvolved ring and lens appear slightly
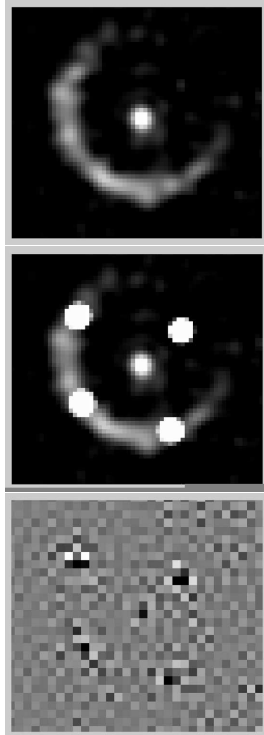
Fig. 10. Results of the last iteration on the synthetic image. *Top*: diffuse background. *Middle*: diffuse background plus point sources. *Bottom*: residual map of the deconvolution.

smoother than the original ones. The largest differences are found under the brightest point source (A), where the deconvolved ring is about 43% below the original one.

Table 3 summarizes the astrometry carried out on this artificial Cloverleaf: the first pair of columns present the measurements made on the final deconvolved image resulting from the iterative process, the second pair of columns the results when using a deconvolved Tiny Tim PSF for a unique deconvolution, and the last one the measurements made on the original image.

The differences between the positions obtained for a particular source reach a maximum of about 0.3 milliarcsec with a mean value around 0.1 milliarcsec, which is slightly better than the internal precision estimated in Table 1. On the other hand, the lens galaxy position is not as accurate: the maximum difference amounts to 20 milliarcsec (i.e. a quarter of a pixel). Indeed, the position of such very faint diffuse objects is rather sensitive to inaccuracies in the PSF: any error in the wings of the bright point source PSFs may have impacts on the faint neighbouring objects.

Given these possible sources of errors and the results of the simulations, we estimate the accuracy on the lens galaxy position to amount to some 20 milliarcsec.

6. Conclusions

We have elaborated a new image–processing method, based on the MCS deconvolution algorithm, which allows, at the same time, to determine the Point Spread Function and to deconvolve a set of images. It is applicable to images which contain at least 2 point sources so that the algorithm can separate the contributions of background objects from those of the PSF itself.

This technique is particularly well–suited to the analysis of multiply imaged quasars: it allows the separation of extended structures (lensing galaxy, arcs or rings) from the point sources. It provides accurate photometry and astrometry, which is very important for modelling the lensed systems.

Our internal error bars on the source positions, taking into account the error coming from the deconvolution only, are of the order of 0.4 milliarcsec. When comparing the astrometry coming from two different sets of images, we find external errors of the order of 1 milliarcsec. They probably find their origin in an incomplete correction of the geometric distortions.

Moreover, we detect the lensing galaxy and measure its position with an accuracy of the order of 20 milliarcsec, and discover a partial Einstein ring, which should allow us to constrain the deflection model and, through inversion of the lens equations, to estimate the light distribution in the quasar host galaxy and narrow line region.

References

Courbin F., Lidman C., Magain P., 1998, A&A, 330, 57
Hazard C., Morton D.C., Terlevich R. & McMahon R., 1984, ApJ, 282, 33
Kneib J.–P., Alloin D. & Pelló R., 1998, A&A, 339, 65
Kris J. & Hook R., 2004, http://www.stsci.edu/software/tinytim
Magain P., Surdej J., Swings J.–P., Borgeest U., Kayser R., Khr H., Refsdal S. & Remy M., 1988, Nature, 334, 6180
Magain P., Courbin F. & Sohy S., 1998, ApJ, 494, 472
Magain P., Courbin F., Gillon M., Sohy S., Letawe G., Chantry V. & Letawe Y., 2006, A&A, in press (astro-ph/0609600)
Noll, K., et al. 2004, "NICMOS Instrument Handbook", Version 7.0, Baltimore, STScI
Turnshek D. A., Lupie O. L., Rao S. M., Espey B. R. & Sirola C. J., 1997, ApJ, 485, L100–111

Glossary

Expression	Definition
Annual parallax	The annual parallax of a celestial body is the apparent displacement of this body viewed from two separated observation points whose base line is the radius of the orbit of the Earth around the Sun. It can also be viewed as the semi-major axis of the apparent ellipse covered by an object on the sky.
Astronomical unit	Semi-major axis of Earth's orbit around the Sun, i.e. 1 AU = 150 10^6 km.
CCD	A charged-coupled device or CCD is an electronic chip sensitive to light. It consists in an integrated circuit containing an array of coupled capacitors, each one of them representing a pixel. Under the control of an external circuit, the charges of a pixel can be shifted to another one. This way, the charges can be transferred row by row to a serial output register. The picture is the display of the electronic distribution.
Hubble constant	Very important concept in cosmology, the Hubble constant is the ratio of the recession speed of a galaxy (due to the expansion of the Universe) to its distance from the observer. The reciprocal of the Hubble constant coincides with the age of the Universe in the case of a model in uniform expansion.

Expression	Definition
Least squares min.	The least squares minimization technique is an approach used in statistics, curve fitting and signal processing amongst others. For given observed data, the least squares values of the unknown factors of a model are the values minimizing the sum of squared deviations, obtained in comparing the data to the model predictions.
Parsec (pc)	Distance of an object having an annual parallax (see definition in the current section) of 1 arcsec, i.e. $1 \text{ pc} = 3.086 \ 10^{16} \text{ m} = 3.26 \text{ LY}$.
Seeing	Blurring and twinkling of observed objects seen through a telescope. It is caused by a combination of temperature differences and turbulences in the atmosphere crossed by the light to reach the detector.
Standard candle	A standard candle is an astronomical object belonging to a special class, such as supernovae or some variable stars. The luminosity of such an object is known due to some characteristics possessed by the whole class. Then, if a distant object is identified as a standard candle, comparing its observed brightness with the luminosity will lead to its distance.
Synchrotron rad.	A relativistic charged particle (most of the time an electron) moving in a magnetic field is accelerated along a field line. In spiraling around the latter, it emits a synchrotron radiation.
Zodiacal light	The zodiacal light is caused by the scattering of sunlight by zodiacal dust.

Bibliography

Adams, T. F. (1974). Variable N galaxies as composite systems. *ApJ* **188**, 463–468.

Barnothy, J. M. (1965). Quasars and the Gravitational Image Intensifier. *AJ* **70**, 666.

Binney, J. & Merrifield, M. (1998). *Galactic astronomy*. James Binney and Michael Merrifield. Princeton, NJ : Princeton University Press (Princeton series in astrophysics).

Blanchet, G. (2006). *Study of the blur, ringing and aliasing artifacts in numerical imaging. Application to restoration*. Ph.D. thesis, Ecole Normale Supérieure de Cachan, France.

Burud, I. (2001). *Gravitational lensing as a tool for determining the age of the Universe*. Ph.D. thesis, Institute of Astrophysics and Geophysics, Université de Liège, Belgium.

Chwolson, O. (1924). Über eine mögliche Form fiktiver Doppelsterne. *Astronomische Nachrichten* **221**, 329.

Courbin, F. (1999). *Deconvolution et combinaison optimale d'images astronomiques: application au cas des mirages gravitationnels*. Ph.D. thesis, Institut d'astrophysique et de géophysique, Université de Liège, Belgium; Observatoire de Paris Meudon - DAEC, France.

Courbin, F., Lidman, C. & Magain, P. (1998). Detection of the lensing galaxy in HE 1104-1805. *A&A* **330**, 57–62.

Courbin, F. & Minniti, D., eds. (2002). *Gravitational Lensing: An Astrophysical Tool*, volume 608 of *Lecture Notes in Physics, Berlin Springer Verlag*.

de Vaucouleurs, G. (1948). Recherches sur les Nebuleuses Extragalactiques. *Annales d'Astrophysique* **11**, 247.

Dickinson, M., Arribas, S., Bergeron, L. E., Boeker, T., Calzetti, D., Holfeltz, S. T., Mobasher, B., Monroe, B., Noll, K., Roye, E., Schultz, A., Sosey, M. & Xu, C. (2002). *HST Data Handbook for NICMOS*, version 5.0, b. mobasher, baltimore, stsci edition.

Eigenbrod, A., Courbin, F., Meylan, G., Vuissoz, C. & Magain, P. (2006). COSMOGRAIL: the COSmological MOnitoring of GRAvItational Lenses. III. Redshift of the lensing galaxy in eight gravitationally lensed quasars. *A&A* **451**, 759–766.

Einstein, A. (1936). Lens-Like Action of a Star by the Deviation of Light in the Gravitational Field. *Science* **84**, 506–507.

Freeman, K. C. (1970). On the Disks of Spiral and S0 Galaxies. *ApJ* **160**, 811.

Hazard, C., Morton, D. C., Terlevich, R. & McMahon, R. (1984). Nine new quasi-stellar objects with broad absorption lines. *ApJ* **282**, 33–52.

Keeton, C. (2004). *gravlens 1.06, Software for Gravitational Lensing: Handbook*. Version 9.

Keeton, C. R. (2001a). A Catalog of Mass Models for Gravitational Lensing. *ArXiv Astrophysics e-prints* .

Keeton, C. R. (2001b). Computational Methods for Gravitational Lensing. *ArXiv Astrophysics e-prints* .

Kneib, J.-P., Alloin, D. & Pello, R. (1998). Unveiling the nature of the Cloverleaf lens-system: HST/NICMOS-2 observations. *A&A* **339**, L65–L68.

Krist, J. & Hook, R. (2004). *The Tiny Tim User's Guide Version 6.3*.

Krolik, J. H. (1999). *Active galactic nuclei : from the central black hole to the galactic environment*. Julian H. Krolik. Princeton, N. J. : Princeton University Press.

Letawe, G. (2006). *Etude spectroscopique de galaxies hôtes de quasars lumineux*. Ph.D. thesis, ULg.

Lynden-Bell, D. (1969). Galactic Nuclei as Collapsed Old Quasars. *Nature* **223**, 690.

Magain, P., Courbin, F., Gillon, M., Sohy, S., Letawe, G., Chantry, V. & Letawe, Y. (2007). A deconvolution-based algorithm for crowded field photometry with unknown point spread function. *A&A* **461**, 373–379.

Magain, P., Courbin, F. & Sohy, S. (1998). Deconvolution with Correct Sampling. *ApJ* **494**, 472.

Magain, P., Surdej, J., Swings, J.-P., Borgeest, U. & Kayser, R. (1988). Discovery of a quadruply lensed quasar - The 'clover leaf' H1413+117. *Nature* **334**, 325–327.

Miller, J. S., French, H. B. & Hawley, S. A. (1978). The spectrum and magnitude of the galaxy associated with BL Lacertae. *ApJL* **219**, L85–L87.

Morgan, N. D., Caldwell, J. A. R., Schechter, P. L., Dressler, A., Egami, E. & Rix, H.-W. (2004). WFI J2026-4536 and WFI J2033-4723: Two New Quadruple Gravitational Lenses. *AJ* **127**, 2617–2630.

Noll, K., Schultz, A., Roye, E., Arribas, S., Bergeron, L., de Jong, R., Malhotra, S., Mobasher, B., Wiklind, T. & Xu, C. (2004). *NICMOS Instrument Handbook for Cycle 14*, version 7.0, baltimore, stsci edition.

Rees, M. J. & Ostriker, J. P. (1977). Cooling, dynamics and fragmentation of massive gas clouds - Clues to the masses and radii of galaxies and clusters. *MNRAS* **179**, 541–559.

Refsdal, S. (1964). On the possibility of determining Hubble's parameter and the masses of galaxies from the gravitational lens effect. *MNRAS* **128**, 307.

Refsdal, S. (1966). On the possibility of testing cosmological theories from the gravitational lens effect. *MNRAS* **132**, 101.

Saha, P. & Williams, L. L. R. (1997). Non-parametric reconstruction of the galaxy lens in PG 1115+080. *MNRAS* **292**, 148.

Schechter, P. L. & Wambsganss, J. (2002). Quasar Microlensing at High Magnification and the Role of Dark Matter: Enhanced Fluctuations and Suppressed Saddle Points. *ApJ* **580**, 685–695.

Schmidt, M. (1963). 3C 273 : A Star-Like Object with Large Red-Shift. *Nature* **197**, 1040.

Schneider, P., Ehlers, J. & Falco, E. E. (1992). *Gravitational Lenses*. Gravitational Lenses, XIV, 560 pp. 112 figs.. Springer-Verlag Berlin Heidelberg New York. Also Astronomy and Astrophysics Library.

Turnshek, D. A., Lupie, O. L., Rao, S. M., Espey, B. R. & Sirola, C. J. (1997). Hubble Space Telescope Observations of the Gravitationally Lensed Cloverleaf Broad Absorption Line QSO H1413+1143: Imaging. *ApJ* **485**, 100.

Walsh, D., Carswell, R. F. & Weymann, R. J. (1979). 0957 + 561 A, B - Twin quasistellar objects or gravitational lens. *Nature* **279**, 381–384.

Williams, L. L. R. & Saha, P. (1999). Pixellated Lenses and Estimates of H_0 from Time-delay Quasars. *ArXiv Astrophysics e-prints* .

Zwicky, F. (1937). On the Masses of Nebulae and of Clusters of Nebulae. *ApJ* **86**, 217.